POLITECNICO DI TORINO

Corso di Laurea Magistrale in Ingegneria Biomedica

Tesi di Laurea Magistrale

Systemic drug co-delivery system with miRNA34a and doxorubicin assembled by layer-by-layer (LbL) for osteosarcoma treatment

Politecnico di Torino

RELATORI

Prof. Piergiorgio Gentile

Prof. Irene Carmagnola

Prof. Chiara Tonda Turo

CANDIDATO

Rebecca Silvestris

A.A. 2022/2023

“So live a life you will remember”

Declaration of Work

I hereby affirm that this dissertation is based on my own efforts and has not been presented in any format for another academic qualification at any university or other institution of higher education. Any information obtained from the published and unpublished works of others has been duly credited within the text and referenced in the bibliography.

Acknowledgements

Firstly, I wish to express my gratitude to Professor Piergiorgio Gentile and Professor Chiara Tonda Turo for affording me the opportunity to undertake this captivating thesis project. Additionally, I would like to extend my appreciation to Irene Carmagnola for her support and guidance throughout my time at both Politecnico di Torino and Newcastle University. Your mentorship has played a significant role in this journey and has solidified my commitment to pursuing a career in research, which I am deeply passionate about. Thank you.

ABSTRACT

Osteosarcoma is a primary malignant bone tumour with elevated mortality rates in youngsters and adolescents. Current therapeutic approaches entail preliminary chemotherapy followed by surgical removal and supplementary chemotherapy. Roughly 30% of patients experience recurrence, underscoring the limitations, as surgery alone cannot effectively manage metastasis. Nanoparticle-mediated targeted drug delivery systems present a promising therapeutic avenue for osteosarcoma, as they overcome the constraints of conven9onal chemotherapy by augmenting retention, permeability, and active targeting.

Objectives

Devise and construct systemic drug co-delivery systems by u9lizing nanoscale modifica9on of miR-34a and doxorubicin via layer-by-layer (LbL) assembly for precise osteosarcoma treatment.

Approaches

PLGA-CS polyplexes were produced using optimized nano-complexation and LbL assembly techniques. LbL-NPs were examined on two-dimensional SaoS-2 and U2OS cell models to gauge metabolic activity and cellular demise via PrestoBlue and Live/dead assessments. Encapsula9on efficiency and drug release kinetics were appraised using the Quan9Fluor® RNA System and UV-VIS Spectroscopy.

Findings

Manufactured PLGA-CS polyplexes exhibited impressive mean encapsula9on efficiencies for miR-34a and doxorubicin, 99.97% and 69.74%, respec9vely. Only the fabricated LbL-NPs P4 and PC4 displayed substantial, sustained release of miR-34a over a ten-day period (P-value 0.002 and 0.011). All LbL-NPs, at concentra9ons of 500 and 1000µg/ml, markedly diminished the metabolic ac9vity of U2OS cells ader five days of incuba9on (P-value <0.001). LbL-NPs P5 and PC5 induced apoptotic activity and cell demise in U2OS cells.

Conclusion

The engineered PLGA-CS polyplexes and LbL-NPs serve as effective nanocarrier systems, inducing cytotoxicity by delivering tumour-suppressing miR-34a and doxorubicin into in vitro osteosarcoma cell models. The incorporation of hyaluronic acid and additional

nanocoating further enhances the cytotoxicity of LbL-NPs against U2OS cells through active targeting.

CONTENTS

1. INTRODUCTION

1.1. BONE TISSUE

“Every change in the form and function of bone or of its function alone is followed by certain definite changes in the bone internal architecture, and equally definite alteration in its external conformation, in accordance with mathematical laws”. This is the Wolf’s low, which states that any changes in the form or function of bone, or solely in its function, result in specific and well-defined alterations in both the internal architecture and external appearance of bones, following mathematical principles. Recent advancements in bone biology, physiology, and orthopaedic research have provided extensive insights into the mechanisms responsible for transmitting mechanical stimuli to bone cells. These mechanisms are vital for the continuous process of bone remodelling, involving various bone cell types such as osteoblasts, osteoclasts, and osteocytes in converting external mechanical signals[16,36]. Additionally, various non-mechanical factors contribute to bone mechanotransduction[62]. A major challenge in the field of biomaterials is to create polymer scaffolds suitable for specific cell types, allowing them to secrete extracellular matrix and form tissue under the right conditions. Bone serves several crucial roles in maintaining bodily functions, including: (1) safeguarding vital organs, (2) offering support and anchorage for muscles involved in movement, (3) producing red and white blood cells for immune defence and oxygenating other tissues, and (4) storing essential minerals like calcium, phosphate, and other ions. Consequently, bone pathologies can have severe consequences, impacting a broad spectrum of bodily functions. Bone deficiencies can arise from abnormal development, tumours, or various types of trauma[56].

Bone is a robust connective tissue characterized by an inner matrix with a honeycomb-like structure, providing it with its inherent strength[58]. The bone tissue consists of various types of bone cells, including osteoblasts and osteocytes, which play roles in tissue formation and mineralization, and osteoclasts, responsible for tissue resorption. Figure 1 illustrates that the mineralized tissue can be categorized into two types based on its structural arrangement: compact (cortical) bone and spongy bone. Compact bone comprises an organic component composed of collagen fibers (ossein) and an inorganic

component containing minerals like calcium, magnesium, and phosphate ions, which collectively form the mineral hydroxyapatite. This mineralized phase, combined with the flexible collagen phase, imparts hardness to the bone without making it brittle. This arrangement forms concentrically organized lamellae, which, in turn, make up osteons, the structural units of compact bone. Collagen fibres are aligned in the same direction within each layer and in various directions between adjacent lamellae. Additionally, bones contain other types of tissue, such as bone marrow, endosteum, periosteum, nerves, blood vessels, and cartilage.

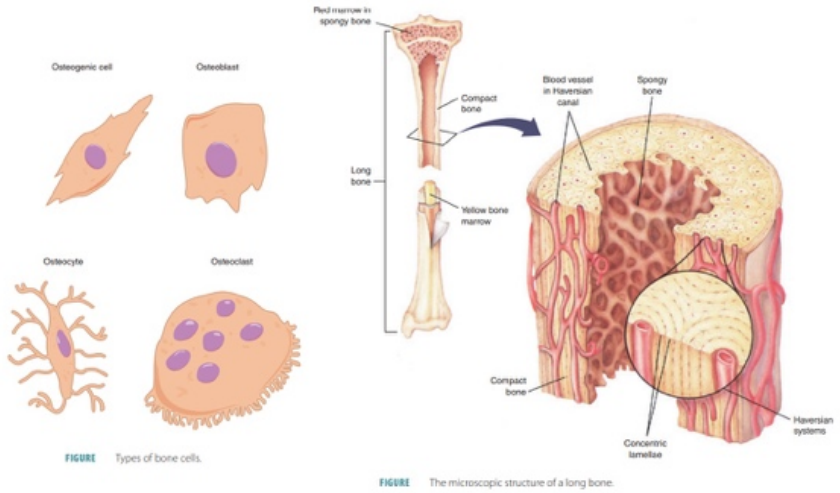

Figure 1: bone tissue structure [93]

1.2. OSTEOSARCOMA: AN ONVERVIEW

Osteosarcoma (OS) is a rare malignant bone tumour, often found in children and young adults, with a bimodal age distribution. It typically occurs in the long bones, such as the femur, tibia, and humerus. OS is known for its heterogeneity, both at the intra-tumoral and inter-individual levels, making it challenging to identify common targetable events. While some cases are associated with inherited cancer syndromes, most OS cases are sporadic[43,59].

Treatment for OS typically involves a combination of chemotherapy and surgery. In recent years, research has focused on understanding the complex molecular and genetic mechanisms associated with OS, as well as its interactions with the bone

microenvironment. This understanding has led to the exploration of potential therapeutic targets to block disease progression.

Among the immune cell population, tumour-associated macrophages (TAMs) play a crucial role in the TME. In most solid cancers, increased TAM infiltration is associated with poor patient prognosis, making them valuable diagnostic and prognostic biomarkers.

Studies have shown that TAMs in OS can have varying effects they can also be implicated in angiogenesis and the activation of intracellular signalling pathways involved in cancer progression.

Osteosarcoma remains a significant clinical challenge, especially in cases with metastatic progression to pulmonary tissue. Despite advances in treatment, the overall prognosis for OS patients is still poor, particularly for those with metastatic disease. Therefore, improving therapy for OS is a major goal for many research and clinical groups worldwide.

One critical aspect of OS research is the tumour microenvironment (TME) is its high degree of heterogeneity, both at the genetic and molecular levels. The bone microenvironment, where OS tumours grow, is a highly dynamic and specialized environment consisting of various cell types, including bone cells (osteoclasts, osteoblasts, osteocytes), stromal cells (MSCs, fibroblasts), vascular cells (endothelial cells and pericytes), immune cells (macrophages, lymphocytes), mineralized extracellular matrix (ECM), chromosomal aneuploidy, mutations, copy number variations, genomic instability, and localized hypermutated regions. Although some genes, such as TP53, RB, MDM2, ATRX, and DLG2, are recurrently mutated in OS, there are still no clear targetable events.

In physiological conditions, these cells engage in paracrine and cellular communication to maintain bone homeostasis.

In OS, tumour cells hijack these physiological pathways to promote their growth and survival. This interaction involves numerous environmental signals, such as cytokines, chemokines, and soluble growth factors, as well as communication through extracellular vesicles (EVs), which serve as vectors for cell-to-cell communication.

One key interaction in OS involves the vicious cycle of bone remodelling between osteoclasts and tumour cells, leading to the release of growth factors from the degraded

bone matrix. EVs secreted by both osteoclasts and OS cells can enhance this cycle. RANK-EVs secreted by osteoclasts may activate RANKL expressed on OS cells, contributing to tumour progression. High levels of RANKL expression in OS biopsy samples have been associated with poor patient outcomes (Figure 2).

Understanding the complex interactions within the OS microenvironment and the role of TAMs in tumour progression is crucial for developing targeted therapies. Current research is exploring multi-kinase inhibitors (MKI) that target both tumour cells and microenvironmental cells. Additionally, the role of EVs as mediators of information transfer in OS biology is gaining attention.

In summary, OS is a challenging bone tumour with a complex genetic landscape and heterogeneous microenvironment. Developing effective therapies for OS requires a deep understanding of these complexities and the identification of potential therapeutic targets within the tumour and its microenvironment (Figure 3).

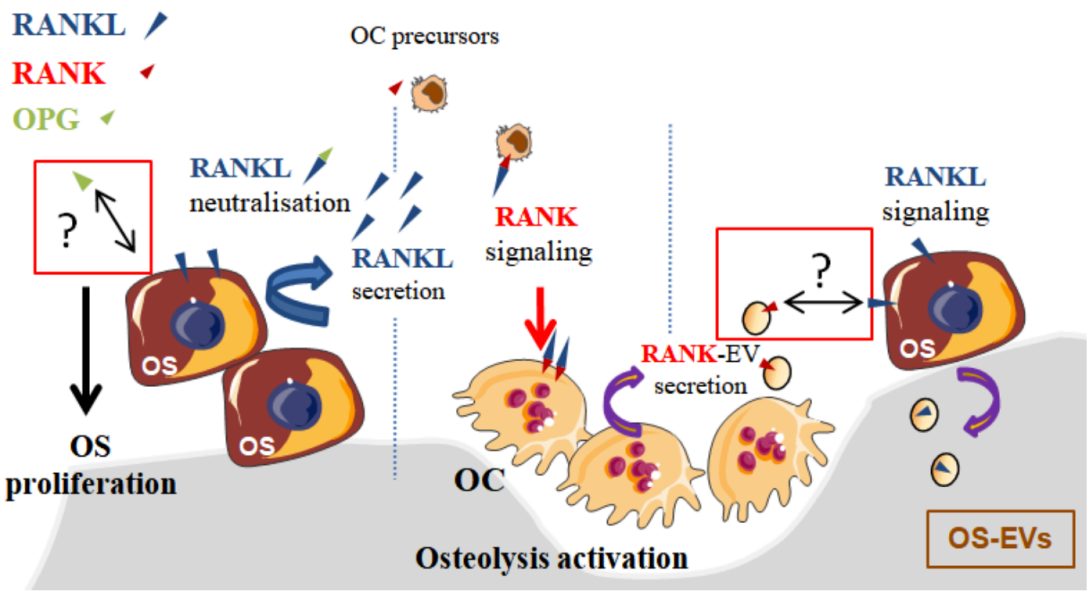

Figure 2: Mechanism of action in OS[9]

Characteristics of Various Bone Cancers

Cancer	Malignant cell origin	Patient demographics[2,3]	Locations (in order of common occurrence)[8]	Sites of metastases
Osteosarcoma	Mesenchymal cells, osteoblasts	Typically five to 25 years of age (median age: 16 years in males, 12 years in females); rare after 60 years of age More common in males and in blacks	Metaphyses of long bones: Distal femur Proximal humerus Proximal tibia Pelvis Skull	Bone, lung
Ewing sarcoma	Unconfirmed; thought to be from primitive stem cells or neural crest cells	Median age: 15 years Slightly more common in males and in whites and Asians	Diaphyses of long bones: Proximal femur Proximal humerus Proximal tibia Pelvis Ribs Scapula	Bone, lung
Chondrosarcoma	Chondrocytes	Typically 40 to 75 years of age Slightly more common in males; no racial predominance	Pelvis Proximal long bones Ribs Scapula Vertebrae	Lungs

Figure 3: Characteristics of different bone tumours[94]

1.3. CONVENTIONAL TREATMENTS & LIMITS

The treatment of osteosarcoma has evolved significantly over the years. Before 1970, the primary treatment was surgical excision, often involving amputations of extremities to achieve clear margins[41]. However, the survival rate for patients with high-grade tumours was less than 20%. In the following two decades, neoadjuvant (preoperative) and adjuvant (postoperative) chemotherapy became effective treatments. Today, the standard approach for osteosarcoma involves neoadjuvant chemotherapy, followed by surgical resection and adjuvant chemotherapy. Radiation therapy is rarely used due to its limited effectiveness and associated risk. The current five-year survival rate for non-metastatic disease is over 70%.

Neoadjuvant chemotherapy aims to shrink the tumour, reduce the number and size of lung metastases, and make limb-salvage surgery more feasible. Adjuvant chemotherapy helps prevent postsurgical metastasis. Effective chemotherapy drugs for osteosarcoma include high-dose methotrexate, doxorubicin (Adriamycin), and cisplatin.

Surgical resection remains the definitive treatment, with the goal of achieving clear margins to minimize recurrence and metastasis; including the "reaction zone" and satellite nodules Advances in preoperative planning, soft tissue surgery techniques, and

the use of endoprostheses have improved the success of limb-salvage surgery. Amputations are still necessary in certain cases with large tumours, compromised vascular structures, or poor response to chemotherapy.

The surgical margin is classified as intra-lesioned, marginal, wide, or radical, depending on the extent of tissue removed. Achieving adequate surgical margins is crucial for prognosis (Figure 4).

Chemotherapy has played a significant role in improving osteosarcoma outcomes. The combination of high-dose methotrexate, doxorubicin, and cisplatin (MAP) has been the most effective regimen for non-metastatic disease, resulting in a 60-70% five-year event-free survival.

Immunotherapy is an emerging field in osteosarcoma treatment, focusing on harnessing the immune system to target tumour cells. Targeted therapies and precision medicine are also being explored to improve treatment outcomes. Genetic studies have identified potential targetable genes and pathways, including the PI3K-mTOR pathway, IGF pathway, VEGF pathway, and others[6].

Several novel approaches are under investigation, such as photodynamic therapy, nanotechnology-based drug delivery systems, and the use of mesenchymal stromal cells for drug delivery. These innovations provide hope for further advancements in osteosarcoma treatment.

In conclusion, the treatment of osteosarcoma has evolved from primarily surgical excision to a multimodal approach involving neoadjuvant and adjuvant chemotherapy, surgical resection, and emerging therapies like immunotherapy and precision medicine. Advancements in surgical techniques and drug regimens have significantly improved survival rates, offering hope for better outcomes in the future.

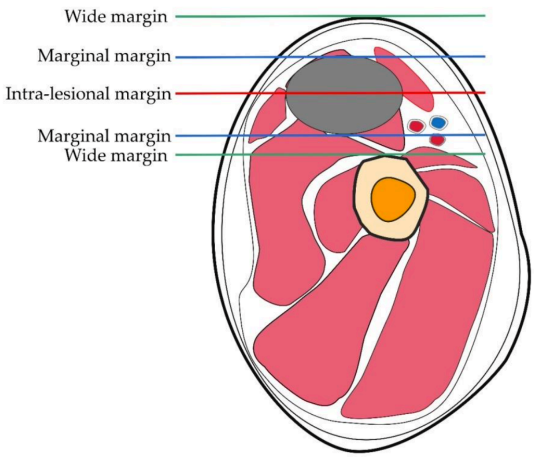

Figure 4: Overview of cancer margin to perform chirurgical treatment[95]

2. POLYMERIC DRUG DELIVERY AS A NEW TECHNOLOGY TO AFFORD OSTEOSARCOMA

Polymeric nanoparticles (Polymeric NPs) in cancer diagnosis and treatment have garnered increasing attention due to their ability to be customized with chemotherapeutic drugs, antibodies, or nucleic acid ligands, enabling them to recognize cancer markers on cell membranes or within cancer cells[42]. They are employed for targeted drug or nucleic acid transport during chemotherapy or gene therapy. Various stimuli such as enzymatic reactions, ultrasound, magnetism, electricity, light, pH changes, and REDOX responses can trigger drug release from these polymeric NPs, making them suitable for transporting drugs to tumour cells.

The development of diverse nanoparticle platforms that allow for size, composition, and functionality adjustments has significantly contributed to the field of nanomedicine. These platforms encompass organic, inorganic, and hybrid nanoparticles. Organic nanoparticles, including synthetic polymers (e.g., polyethyleneimine, polyethylene glycol), synthetic hydrogels (e.g., polyacrylamide), natural polymers (e.g., chitosan, hyaluronic acid), and degradable polymers (e.g., collagen, polylactic acid), have been widely explored. These polymer-based nanoparticles can passively carry cargo or release it in response to specific triggers[12].

Nanoparticle-based drug delivery systems (Figure 5) offer new possibilities for overcoming limitations associated with traditional drug therapies, providing both therapeutic and diagnostic functions[2]. The efficiency of drug or gene delivery depends on the physical and chemical properties of the delivery platform, along with physiological constraints like clearance by the mononuclear phagocyte system and extravasation from circulation at tumour sites through the enhanced permeability and retention effect.

The application of nanotechnology in cancer therapy, known as cancer nanotechnology, holds promise in early diagnosis, prediction, prevention, personalized therapy, and medicine. It emphasizes target-specific drug therapy and early pathology diagnosis. Various nanocarrier systems have been developed for cancer treatment, including antibody-conjugated nanoparticles, nuclear drug delivery systems, and controlled drug release formulations.

Combination therapy, which combines multiple therapeutic agents to enhance anticancer effects while reducing toxicity and drug resistance, has gained popularity. Nanotechnology-based combination drug delivery systems have emerged as effective strategies to overcome biological barriers and enable controlled, targeted delivery of chemotherapeutic drugs, achieving enhanced anticancer effects with reduced side effects[51].

To address the challenges of conventional chemotherapy, nanotechnology offers opportunities to optimize drug delivery, reducing toxic side effects. Nanocarriers, including liposomes, dendrimers, micelles, carbon nanotubes, polymer-drug conjugates, and nanoparticles (NPs), can protect drugs from degradation, enable transport through biological barriers, and increase drug availability at targeted sites. Combination drug delivery using various types of nanoparticulate systems is a frontier in cancer research, showing significant therapeutic potential.

The role of biodegradable polymeric NPs in drug delivery is the basis for cancer treatment, particularly targeting osteosarcoma. Surface modifications with ligands allow these NPs to target specific receptors on cancer cells. Various polymer-based drug delivery systems have been developed and tested in preclinical and clinical settings, with promising results.

In summary, the significance of polymeric nanoparticles and various nanoparticle platforms in cancer diagnosis and treatment is a new important challenge. Nanotechnology-based drug delivery systems offer opportunities to enhance therapeutic outcomes while minimizing side effects, making them a promising avenue for future cancer therapies.

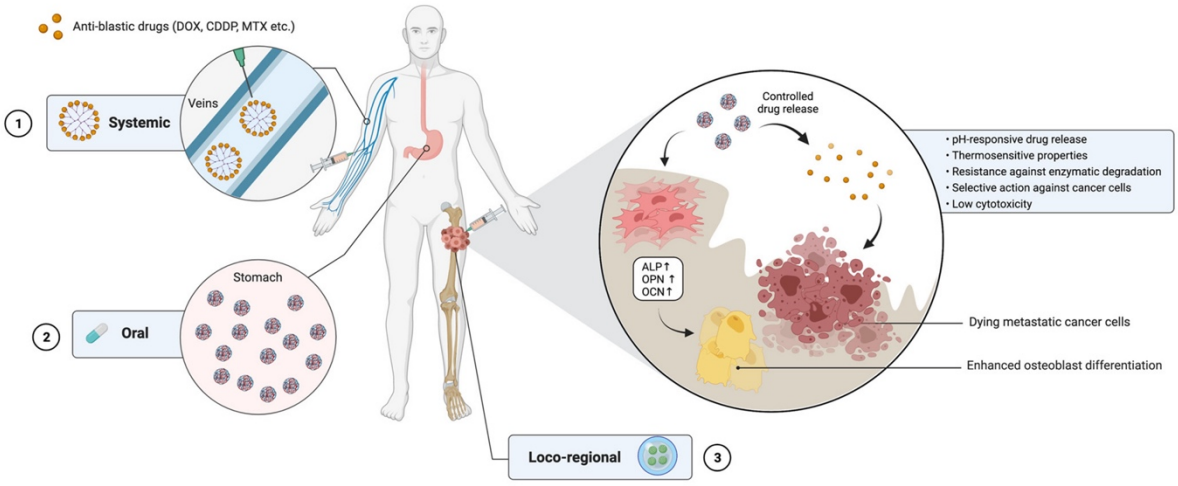

Figure 5: Different polymeric drug delivery in human beings[2]

2.1. POLIPLEXES: STATE OF THE ART

Various types of polymers, including synthetic, natural, and microbial polymers can be used for targeted drug delivery in cancer treatment. These polymers are harnessed to create tailored drug delivery systems with specific properties suited for their intended applications.

Biodegradable polymers have emerged as key materials for designing safe and efficient drug carriers aimed at delivering therapeutic agents selectively to cancer cells. These polymeric carriers are employed for both systemic targeting and localized drug delivery. Their tunable physicochemical characteristics, high loading capacity, and extensive research in polymer chemistry have led to the development of diverse systems for polymer-based drug delivery.

These systems include polymeric nanoparticles, polymeric micelles, polymerosomes, polyplexes, polymer-lipid hybrid nanoparticles, polymer-drug/protein conjugates, and dendrimers, all intended for systemic drug targeting (Figure 6). These polymeric nanosystems are typically administered intravenously, enabling them to target tumour masses effectively. Surface modifications, such as PEGylation or ligand functionalization, can provide long-term circulation of the drug carriers in the bloodstream. The coupling of low molecular weight drugs to polymers enhances stability in the bloodstream and promotes localization in the tumour site by taking advantage of extended circulation times.

These localized systems offer advantages like controlled and prolonged drug release in cancer cells, one-time administration, and the avoidance of systemic exposure to anti-neoplastic agents.

The primary strategy for targeting anti-cancer drugs using polymeric carriers relies on blood circulation and the extravasation effect, often referred to as passive targeting. Active targeting involves attaching ligands like monoclonal antibodies, aptamers, cell-specific peptides, carbohydrates, and small molecules to the polymeric nano-systems. These ligands target specific receptors overexpressed on tumour cells. Additionally, stimuli-responsive carriers release drugs in response to external stimuli or intrinsic features of cancerous tissues, such as pH and hyperthermia. Intracellular drug targeting focuses on delivering drugs to specific cellular compartments, while intratumorally drug targeting involves direct injections into tumors or the placement of drug-containing millirods or wafers after surgical tumour resection. Tumor vasculature drug targeting is achieved by coupling anti-angiogenic drugs to polymers like PEG and HPMA.

In summary this is an overview of the diverse applications of polymers in cancer drug delivery, highlighting their role in both systemic and localized targeting strategies, as well as their responsiveness to various stimuli for precise drug release. These polymer-based drug delivery systems hold significant potential in improving the effectiveness and safety of cancer treatment.

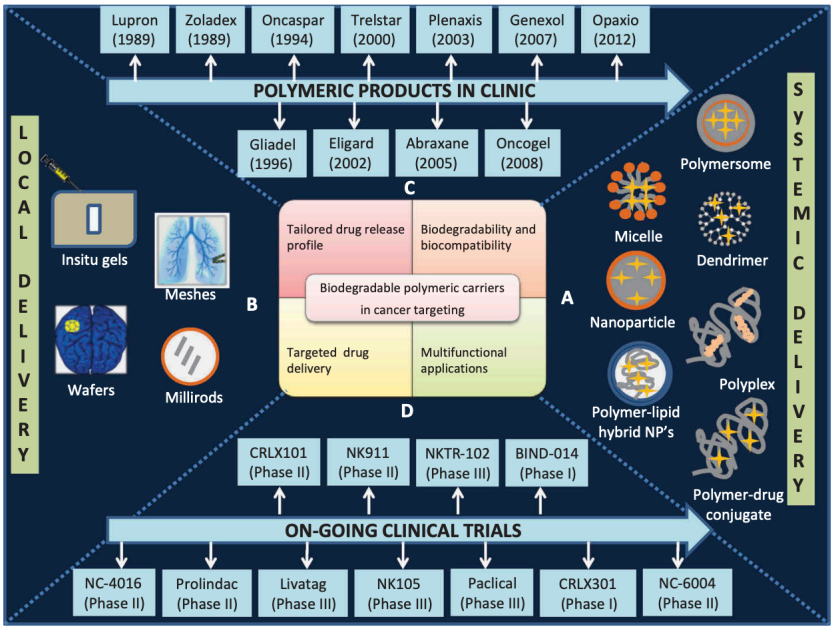

Figure 6: Overview of polymeric products in trial and in use[96]

2.2. OSTEOSARCOMA COMBINATION THERAPY

2.2.1. MIRNA IN CANCER

MiRNAs are small noncoding RNAs that play a complex role in posttranscriptional gene expression and have the potential to serve as diagnostic, prognostic, and therapeutic tools in cancer, including OS[8,39]. While the molecular mechanisms underlying skeletal sarcomas like OS are not fully understood, miRNAs have emerged as crucial players in cancer biology, acting as both oncogenes and tumour suppressors, they also have an high diagnostic potential.

Immunotherapy approaches, such as dendritic cell (DC) therapy and cytokine therapy, have shown promise in preclinical and clinical studies. Targeting tumour stem cells (TSCs) is another area of investigation in OS treatment, as these cells are associated with tumour progression, recurrence, and chemoresistance.

The role of microRNAs (miRNAs) in various diseases can be summarized in this way[47,72,73]:

1. Discovery of miRNA's Role in Disease: In 2002, it was discovered that dysregulation of miRNAs could contribute to the development of chronic lymphocytic leukemia. This discovery led to increased research into the role of miRNAs in various diseases, including cardiovascular diseases, fibrosis, diabetes, neurodegenerative diseases, and cancer. This dysregulation of miRNAs make them promising candidates for further exploration in skeletal sarcomas.

2. Dual Role of miRNAs in Cancer: MiRNAs can function as either oncogenes (onco-miRs) or tumour suppressors in cancer, depending on their specific mRNA targets within tumour cells.

3. Extracellular and Circulating miRNAs: MiRNAs have been found in various bodily fluids, including blood, saliva, and urine. They are highly stable in these fluids and are often packaged into exosomes, small vesicles released by cells. Researchers have identified

specific miRNA expression profiles in both serum and bone tissue, providing a basis for diagnosing and monitoring OS. Various miRNAs, including miR-124, miR-221, miR-101, miR-375, miR-144-3p, miR-215-5p, and others, have been found to be differentially expressed in OS patients compared to healthy individuals.

4. Potential of Circulating miRNAs as Biomarkers: Scientists are exploring the use of miRNAs found in circulating exosomes as biomarkers for different diseases. These miRNAs can potentially serve as diagnostic biomarkers, prognostic, and disease surveillance tools and their expression levels correlate with disease stage, metastasis, and patient prognosis.

5. Methods for miRNA Detection: Several methods for miRNA analysis have been developed, including amplification-based, hybridization-based, microarray, capillary electrophoresis-mass spectrometry, and label-free miRNA electrochemical biosensors. Standardization of miRNA analysis methods is a challenge that needs to be addressed.

6. Therapeutic Potential: MiRNAs play diverse roles in both normal and disease conditions. Some miRNAs act as tumour suppressors by targeting oncogenes, while others promote cancer progression. This knowledge has led to the development of therapeutic molecules that can modulate miRNA activity. MiRNAs also play a role in OS treatment, particularly in relation to chemotherapy and radiotherapy. Some miRNAs, such as miR-328-3p and miR-513a-5p, have been shown to enhance the sensitivity of OS cells to radiation therapy. In terms of chemotherapy, miRNAs like miR-19a-3p, miR-92a, miR-34a, miR-29 family, miR-590-3p, and miR-340 have been associated with chemosensitivity and chemoresistance in OS cells (Figure 7). Modulating these miRNAs may offer a potential avenue to improve the efficacy of chemotherapy for OS patients.

7. Role of miRNAs in Bone Development: MiRNAs also play a role in bone development, influencing processes like osteoblastogenesis and osteoclastogenesis, osteosarcoma, and their association with cancer progression. Various miRNAs have been identified as either promoters or inhibitors of these processes. Several miRNAs have been associated with primary bone tumors, including Ewing's sarcoma, chondrosarcoma, osteosarcoma,

and giant cell tumors, and their expression patterns change during tumour progression. In osteosarcoma, new oncomiRs (tumour-promoting miRNAs) have been identified, including miR-21, miR-92b, miR-603, miR-130a, miR-488, miR-301a, miR-9, and miR-130b.

These findings suggest that miRNAs play crucial roles in bone development and cancer progression, including osteosarcoma[47].

In summary, miRNAs have emerged as important regulators of gene expression in both health and disease. They have the potential to serve as diagnostic tools, therapeutic targets, and biomarkers for various conditions, including cancer and bone-related disorders[4,50,64].

miRNA type	Relative level in OS tissues	Pathway involved	Effect of miRNA
miRNA-128	Increased	PTEN/AKT signaling pathway	Enhances the metastasis and invasion of OS cells
miRNA-23a	Increased	PTEN signaling pathway	Enhances the metastasis and invasion of OS cells
miRNA-543	Increased		Inhibits the function of PRMT9 protein, stabilizes HIF-1α protein, and promotes the proliferation and glycolysis of OS cells
miRNA-146b-5p	Increased		Promotes OS cell invasion and metastasis by ZNRF3
miRNA-374a	Increased		Promotes the proliferation of OS cells by targeting the expression of AXIN2 functional proteins
miRNA-34a	Reduced	Notch signaling pathway	Affects the transcription of P53 gene and downregulates c-MET gene to inhibit the proliferation and metastasis of OS cells
miRNA-143, miRNA-145, and miRNA-200b/c	Reduced	Notch signaling pathway	Inhibit the proliferation and metastasis of OS cells
miRNA-34c	Reduced	Notch signaling pathway	Directly inhibits the normal differentiation of osteoblasts, leading to a cell cycle regulation disorder
miRNA-191	Increased		Risk factors for short-term mortality and related to distant metastasis
miRNA-221	Increased		Related to distant metastasis and high tumor clinical stage
miRNA-27a	Increased		Related to higher clinical stage, distant metastasis ($P = 0.01$), and poor response to chemotherapy
miRNA-17-5p	Increased	BRCC2-dependent signaling pathway	Promotes OS proliferation
miRNA-126	Reduced		Associated with higher TNM staging, shorter overall survival time
miRNA-106b	Reduced	PI3K/AKT signaling pathway	Regulates cell cycle G1/S transformation and regulates the invasion ability of U2OS OS cells
miR-223	Reduced	JNK signaling pathway	Negatively regulates the expression of Hsp70 in OS cells treated with cisplatin and produces drug resistance of cisplatin
miRNA-218	Reduced	Three major regulatory target genes are metastasis factor 1, matrix met alloproteinases (MMP)-2 and MMP-9	Involved in the invasion and metastasis of OS
miRNA-199a-5p	Increased		Serves as an indicator of efficacy evaluation
miRNA-300	Increased		Shows higher recurrence, metastasis, and poor response to chemotherapy, poor prognosis
miRNA-1908	Increased		Shows prognostic factors affecting the overall survival of OS patients
miRNA-195-5p and miRNA-199a-3p	Increased		Offers distant metastasis
miRNA-320a	Increased		Associated with biopsy staging
miR-150	Reduced		Acts as an anti-cancer regulator and acts on ZEB1 to inhibit the development of OS
miR-208b	Reduced		Downregulates the expression of ROR2 (receptor tyrosine kinase-like orphan receptor 2) gene, it can be used as a new target to prevent tumor metastasis
miR-210	Increased		Involved in hypoxia and promotes the differentiation of OS cells by activating TGF-β1 and its downstream factors, thereby promoting the tumor development and metastasis
miR-27-3p	Increased		Inhibits the anti-cancer effect of ING5 and promotes the proliferation of OS cells

miRNA type	Relative level in OS tissues	Pathway involved	Effect of miRNA
miR-133b	Increased		Enhanced drug resistance of tumor cells to cisplatin, it can be used as a biomarker for detecting whether or not drug resistance is produced
miR-340	Decreased		Increases drug resistance behavior in OS, it can be used as a biomarker to alleviate the drug resistance of OS
miR-25-3p	Increased		Used as an important non-invasive biomarker for patient OS monitoring and prognosis assessment
miR-199a-3p	Decreased		Increases the growth as well as the development of OS

Figure 7: Summary of important miRNA type associated with OS[72]

2.2.2. MIR34a

MiR-34a, a microRNA play a crucial role in osteosarcoma. This microRNA is a direct target of the tumour suppressor gene p53 and plays a pivotal role in regulating numerous cellular processes, including cell cycle control, senescence, and apoptosis.

MiR-34a has a negative regulatory effect on osteosarcoma by inhibiting cell proliferation, migration, and invasion. It also highlights its role in targeting Sox-2, a transcription factor critical for osteosarcoma cell self-renewal and tumorigenesis[67].

Recent studies have demonstrated that MiR-34a, along with its family members miR-34b and miR-34c, is downregulated in osteosarcoma stem-like cells (OSCs) and osteospheres[74]. The introduction of miR-34a mimics and short hairpin RNA targeting Sox-2 mRNA (shSox-2) effectively reduces the transformation properties of human OSCs in vitro and their ability to form tumors in soft agar. Furthermore, miR-34a and shSox-2 epigenetically suppress the expression of stem cell markers, including stem cell antigen-1 (Sca-1), ultimately hindering osteosphere formation.

miR-34a is a direct regulator of Sox-2, which not only influences proliferation and metastasis but also the self-renewal capacity of OSCs. It suggests that miR-34a's inhibitory effect on osteosarcoma tumour growth and metastasis is linked to its ability to reduce self-renewal capacity, eliminate tumorigenic potential, and impede invasion in vitro.

Furthermore, it is necessary to focus on the relationship between miR-34a, p53, and osteosarcoma. miR-34a is highlighted as a transcriptional target of p53 and an essential factor in p53-dependent cellular processes such as cell cycle arrest and apoptosis. Overexpression of miR-34a is found to inhibit the growth and metastasis of osteosarcoma cells both in vitro and in vivo[46].

Some studies also investigates the response of osteosarcoma cells to etoposide, an antitumor drug. The results indicate that wt-p53 cells induce p53-dependent miR-34a expression upon etoposide treatment, leading to cell cycle arrest in the G1 phase and downregulation of CDK4. In contrast, p53-deficient cells exhibit a different response, with cell cycle arrest in the G2/M phase.

Moreover, the role of miR-34 family members, including miR-34a, is important in suppressing cancer growth by targeting various genes involved in cell cycle regulation, apoptosis, and DNA repair.

In summary, the importance of miR-34a is founded in regulating osteosarcoma by targeting Sox-2 and highlights its association with p53-mediated processes. It suggests that enhancing miR-34a expression could be a potential therapeutic strategy for treating osteosarcoma and also it has an impact in inhibiting cancer growth by targeting key genes involved in tumorigenesis[63,37].

2.2.3. DOXORUBICIN (DOX)

Doxorubicin is one of the most effective drugs for the first-line treatment of high-grade osteosarcoma, specifically in the case of metastatic cancer.

DOX is a potent but cardiotoxic drug, limiting its use.

Conventional anticancer drugs[71] like DOX are limited in efficacy due to their lack of specific targeting and associated high doses, leading to side effects. Nanotechnology offers a potential solution to overcome these limitations by delivering DOX in nanoparticles (NPs), to enhance drug delivery and efficacy (Figure 8): they loaded DOX into nanoscaled, injectable, and non-toxic drug delivery systems designed to have high specificity for bone tissue using a bisphosphonate (BP)[57]. The goal was to improve the preferential accumulation of DOX at the site of osteolytic metastases, taking advantage of BP's strong binding to bone tissue. Previous studies had characterized NPs made of a conjugate between PLGA and ALE, demonstrating their biocompatibility and binding to hydroxyapatite.

The drug loading procedure did not affect the optimal properties of the NPs. Subsequently, the researchers investigated the intracellular uptake of DOX into tumour cells when delivered by the NPs compared to the free drug. They observed clear nuclear accumulation of DOX in most tumour cell lines, indicating its effectiveness.

It was also evaluated the antitumor effects of DOX-loaded NPs in a mouse model of bone metastases induced by human breast carcinoma cells (MDA-MB-231). The results showed that DOX-loaded NPs effectively reduced the incidence of metastases compared to unloaded NPs and free DOX. The reduction in the incidence of metastases was more

pronounced with the highest dose of DOX-loaded NPs. Importantly, the treatment did not induce severe toxicity in the bone marrow, likely due to the low doses of DOX used.

It is necessary to analyze the specific case of doxorubicin resistance in osteosarcoma and the potential of H2S-releasing doxorubicins (Sdox) to overcome this resistance. Sdox was found to preferentially accumulate within the endoplasmic reticulum (ER) and induce ER-dependent apoptosis in osteosarcoma cells, including those with doxorubicin resistance. Sdox's mechanism of action involves sulfhydration of ER-associated proteins, leading to their ubiquitination and degradation. This unique property of Sdox makes it a promising candidate for further evaluation in preclinical models of osteosarcoma, especially in cases of doxorubicin resistance[5].

So finally we can focus on the potential of nanocarrier-based drug delivery systems and innovative approaches like H2S-releasing doxorubicins that improve the effectiveness of anticancer treatments, especially in cases of drug resistance and metastatic bone cancer. These advancements offer hope for more targeted and less toxic cancer therapies in the future.

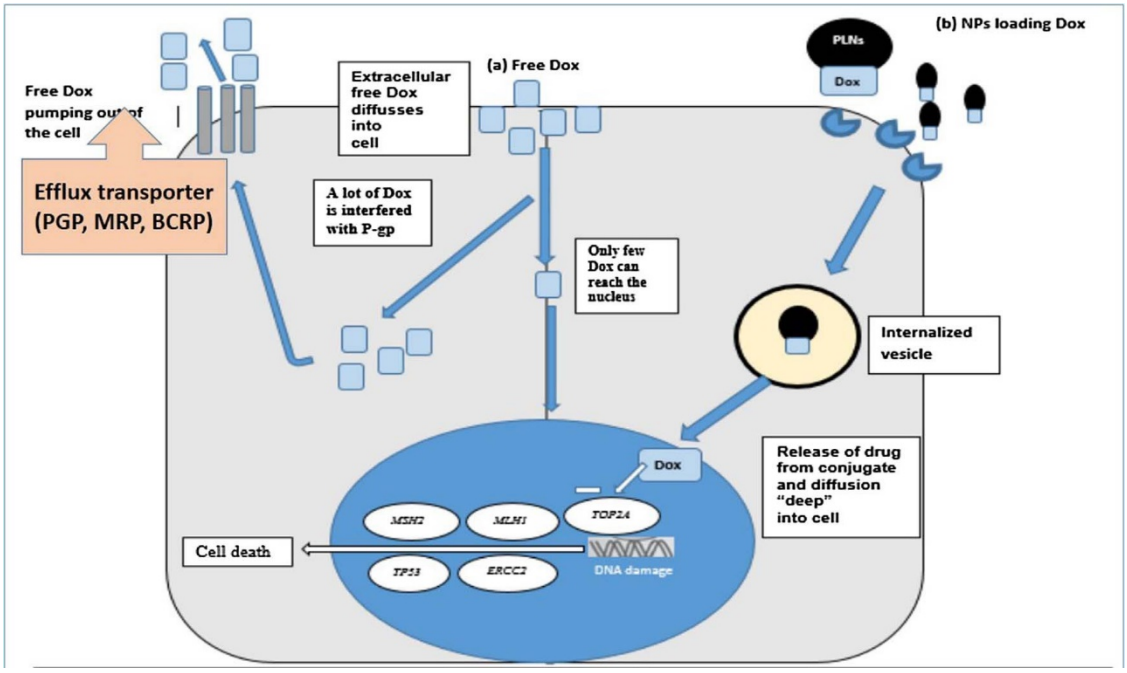

Figure 8: DOX internalization into cell[61]

2.2.4. CURCUMIN

The dietary phytochemical curcumin, derived from the rhizomes of Curcuma longa, has been used in traditional medicine for its diverse therapeutic properties. It has been employed to treat various conditions, including inflammation, skin lesions, coughs, rheumatism, hepatic dysfunction, and bacterial and fungal infections.

Curcumin is a polyphenol with the chemical formula C21H20O6 and a molecular weight of 368.38. Its potential therapeutic benefits have been demonstrated in a wide range of chronic diseases, including cancer, with particular attention to its application in the treatment of osteosarcoma.

Curcumin is known for its various biological activities, including anti-inflammatory, antioxidant, cytotoxic effects on human osteosarcoma cell lines, including U2OS, MG-63, and Saos-2 and anticancer properties (Figure 9). It has been studied for its potential to inhibit tumour growth, angiogenesis, and induce apoptosis (cell death) in cancer cells[27]. Specifically, curcumin increases the levels of the transcription factor p53 while simultaneously reducing the levels of Sp1, another transcription factor. These factors play a crucial role in regulating cellular pathways that lead to apoptosis. Curcumin also affects the expression of their target genes, including DNA methyltransferase 1 (DNMT1) and growth arrest and DNA damage-inducible 45 alpha gene (Gadd45a).

While curcumin holds promise as a therapeutic agent for various cancers, its limited stability and poor bioavailability after ingestion have led to the search for structural analogues with improved properties.

In conclusion, Curcumin, either alone or in combination with other agents, holds promise as an effective cancer therapy, particularly in the context of osteosarcoma[33,69].

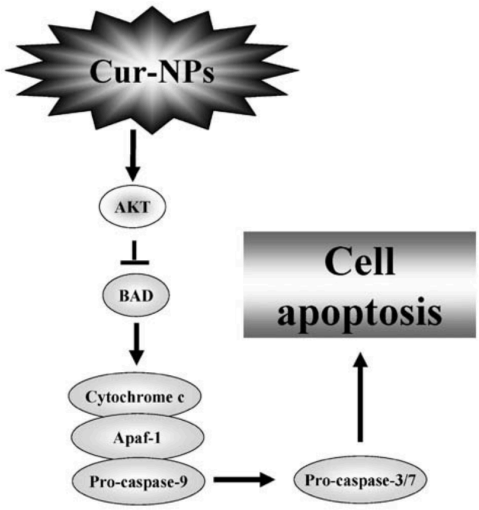

Figure 9: Schematic diagram of Cur-NPs regulating the apoptotic signaling pathway in human osteosarcoma U2OS cells[52]

2.3. LBL COATING TECHNIQUE

Layer-by-layer (LbL) self-assembly is a versatile technique utilized for creating functional surface coatings, particularly under aqueous assembly conditions. LbL assembly involves the sequential deposition of multivalent compounds with complementary interactions, resulting in the formation of a multilayered structure (Figure 10). Initially applied to charged colloids, the use of LbL gained significant attention when it was adapted for polyelectrolytes in 1991. This technique offers various advantages, especially in biomedical applications, as it allows for the gentle and conformal coating of substrates with diverse physicochemical properties and geometries without causing damage. LbL assembly can efficiently coat large surface areas while maintaining nanoscale resolution, which is crucial for precise control over biological surface interactions. Additionally, its mild, aqueous assembly conditions enable the incorporation of small molecules and biological agents without compromising their stability.

The applications of LbL in biomaterials are extensive, encompassing cellular engineering, tissue engineering, biosensors, antimicrobial materials, vaccines, drug delivery systems, and more (Figure 11). It is necessary to underscore how the modularity of LbL assembly has been leveraged to create multifunctional delivery systems that enhance treatment efficacy, improving biological performance and targeting specific tissues.

LbL assembly primarily relies on electrostatic interactions between oppositely charged compounds, although other forces like hydrophobic interactions, hydrogen bonding, covalent bonding, and more can also contribute to film growth. Various methods have been employed for multilayer assembly, including dipping, spraying, spin coating, electromagnetic assembly, 3D printing, and micropatterning. Polyelectrolytes, both synthetic and naturally derived, are commonly used building blocks, but other macromolecules, nanoparticles, and inorganic materials can also be incorporated.

The growth and stability of LbL films are influenced by assembly parameters such as temperature, ionic strength, pH, molecular weight, species concentration, incubation time, and assembly method.

It enables the encapsulation of diverse therapeutic cargo, from small molecules to nucleic acids to large macromolecules like proteins and cells. The loading capacity can be tailored based on the molecule's characteristics and desired release profile. Additionally, LbL films protect cargo from environmental factors, prolong shelf-life, and minimize toxicity.

In summary, Layer-by-layer self-assembly is a versatile technique with numerous applications in biomaterials, including drug delivery. Its modularity, gentle assembly conditions, and ability to tailor properties make it a powerful tool in the development of advanced biomaterials and drug delivery systems[44,22].

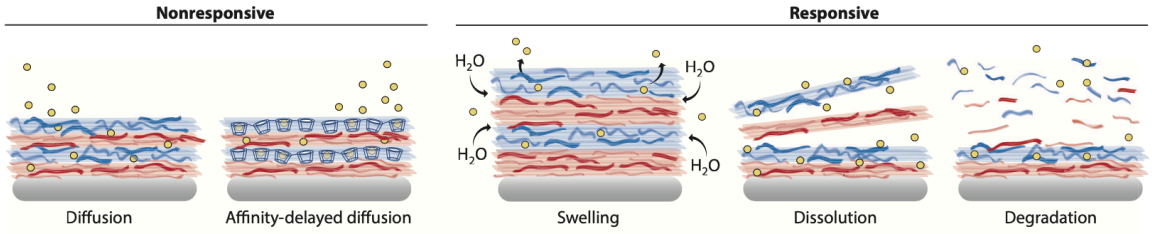

Figure 10: LBL technique[1]

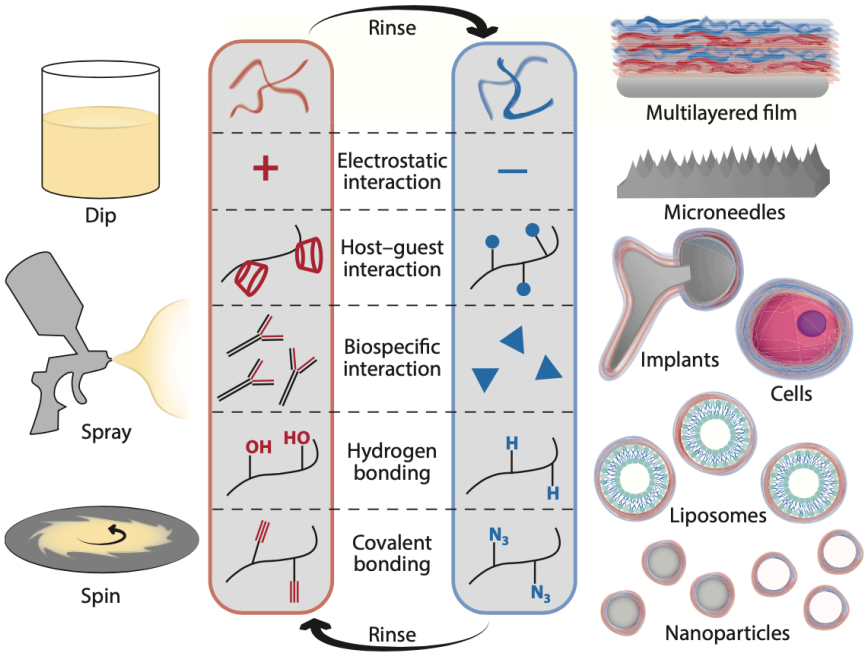

Figure 11: LBL application in different fields[1]

2.3.1. POLYELECTROLITES MATERIALS

2.3.1.1. CHITOSAN

Chitosan (Figure 12), a natural polysaccharide, has garnered substantial scientific interest over the past two decades due to its biocompatibility and chemical versatility. Chitosan's -NH2 groups and varying molecular weights have made it a valuable material in drug delivery and tissue engineering, holding promise for various healthcare applications.

Chitosan-based nanocarriers have gained attention due to their biodegradability, biocompatibility, non-toxicity, and low immunogenicity. The presence of glucosamine groups imparts a positive charge to the carrier, enhancing drug delivery. Chitosan can also interfere with tumour cell metabolism, inhibiting cell growth or inducing apoptosis. N-trimethyl chitosan (TMC), a quaternized chitosan derivative, offers aqueous solubility and tunable biodegradability. Physical crosslinking using negatively charged ions like tripolyphosphate (TPP) forms stable nanoparticles, preventing toxicity and undesirable effects. Modifying nanoparticles with Pluronic block copolymers can enhance their anticancer properties.

Chitosan's cationic nature makes it suitable for forming particles with anionic polymers to encapsulate microRNA (miRNA) or create polyplexes[32,68]. Fine-tuning chitosan characteristics is crucial for successful formulations. It is also investigated chitosan miRNA formulations in the last decade, highlighting differences in materials, formulation processes, and intended applications. Factors contributing to optimized systems' superiority are also discussed to maximize the potential of chitosan miRNA nanocarriers. Chitosan is increasingly used for safe nucleic acid delivery in gene therapy due to its bioadhesive, low toxicity, biodegradability, and biocompatibility. Chitosan can be modified to enhance solubility and stability of chitosan-nucleic acid complexes, improve target cell delivery, and facilitate intracellular processes like endosomal escape, unpacking, and nuclear import of expression plasmids.

In summary, chitosan's unique properties make it a valuable material in drug delivery, tissue engineering, and gene therapy[29,11].

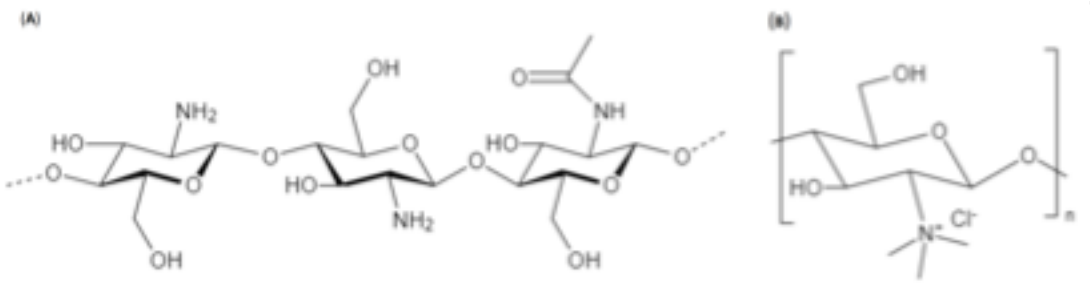

Figure 12: Chitosan structure[20]

2.3.1.2. PECTIN

Pectin is a complex polysaccharide naturally present in plant cell walls and can be efficiently extracted from edible plant materials such as sugar beet, citrus peel, and apple pomace. It is composed of partial methyl esters of polygalacturonic acid and their salts, with molecular weights reaching approximately 200 kDa. Pectin is classified into two main types: high methoxy pectin (> 50% DE) and low methoxy pectin (< 50% DE).

Pectin has gained attention for its potential use as a colon-selective drug delivery carrier due to its ability to prolong retention in the upper gastrointestinal tract and undergo degradation by colonic enzymes. Numerous studies since the 1990s have explored pectin's applications in drug delivery and its potential for targeting the colon.

One of the focuses of research involves redox-responsive microbeads containing thiolated pectin-doxorubicin (DOX) conjugate coated with an enteric polymer. The in vitro and in vivo anticancer efficacy of these microbeads, along with their specificity for the target site, is being evaluated. Pectin's complex structure and various biological activities make it a versatile material.

In conclusion, pectin has demonstrated anti-metastatic properties in various malignancies. Its ability to inhibit galectin-3, which is overexpressed in cancer, has been a key focus of research. Pectin's well-tolerated nature has led to its exploration in clinical settings for conditions like B-chronic lymphocytic leukemia relapse[24].

2.3.1.3. HYALURONIC ACID

Hyaluronic acid (HA) is a linear mucopolysaccharide composed of alternately repeated N-acetylglucosamine and glucuronic disaccharide units. It is a major component of the extracellular matrix and has hydroxyl and carboxylic groups, as well as an N-acetyl group, which makes it amenable to various chemical modifications. HA possesses several advantageous properties, including a high water-binding capacity, nontoxicity, biodegradability, cytocompatibility, and nonimmunogenicity. These attributes have led to significant interest in developing HA-based nanomaterials for various biomedical applications, particularly in drug delivery systems (DDS) and molecular imaging.

Many cancer cells are known to overexpress HA-binding receptors, including CD44, LYVE-1 receptors, and RHAMM. Overexpression of CD44 receptors has been observed in various cancer cell types, such as those found in colon, ovarian, breast, and squamous carcinoma.

HA has been frequently modified with drug carriers to improve drug delivery to cancer cells that overexpress CD44. HA is commonly used in nanoparticle (NP) formulations (Figure 13), which leverage the enhanced permeability and retention (EPR) effect in tumour areas. By conjugating HA to the surface of NPs, researchers can enhance the selectivity of drug delivery to cancer cells through active targeting.

The HA-CD44 binding pair is well-characterized and suitable for investigating ligand functionalization and presentation. HA binds avidly to the CD44 cell-surface receptor, facilitating cell targeting and internalization. Researchers have used this interaction to

create stable layer-by-layer (LbL) NPs that target cell-surface CD44. These NPs have demonstrated increased circulation half-lives and enhanced tumour accumulation, particularly in ovarian cancers that overexpress CD44.

In summary, HA-based nanomaterials hold promise for cancer therapy, especially in targeting cancer cells that overexpress CD44 receptors. These nanomaterials can be tailored for drug delivery and imaging applications, offering potential advancements in cancer treatment[13].

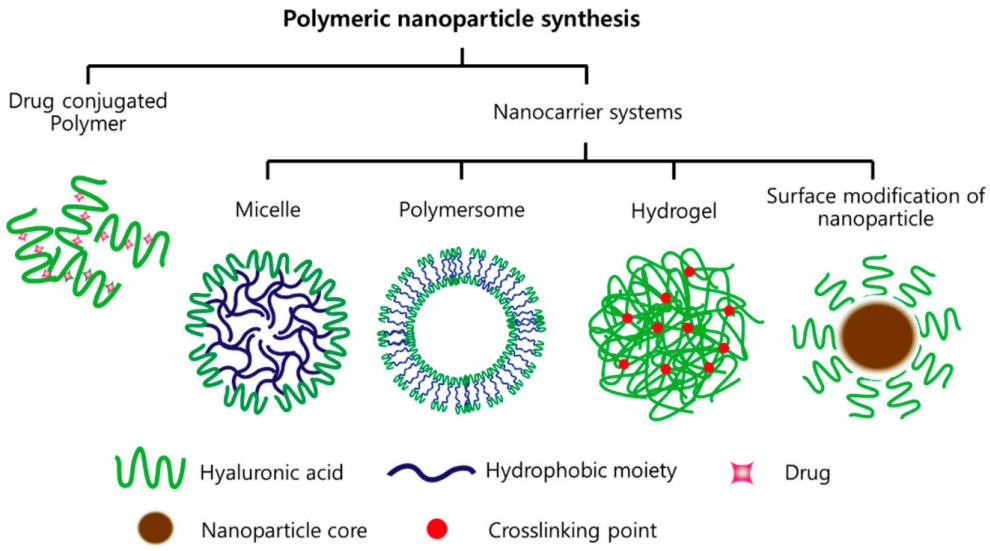

Figure 1. Formulations of hyaluronic acid (HA)-based nanomaterials.

Figure 13: Formulation of hyaluronic acid (HA)-based nanomaterials[30]

2.4. ADVANTAGES OF THE INTERACTION BETWEEN MATERIALS

2.4.1. Mir34 / CHITOSAN / PLGA

In this section is evaluated the potential of combining together these different materials to reach an efficient formulation of NPs, these nanoparticles are designed to enhance the targeted delivery of miR-34a.

It is focused to the development of LbL nanoparticles with a biodegradable poly(lactic-co-glycolic acid) (PLGA) core. This choice is significant because PLGA is an FDA-approved biocompatible polymer that can degrade into lactic acid and glycolic acid, both easily metabolized by the body. This characteristic reduces the risk of systemic toxicity

associated with nanoparticle-based drug delivery systems. Additionally, the tunable size and controlled RNA release offered by LbL nanoparticles make them suitable for precise drug delivery.

There are some advantages of using PLGA-based LbL nanoparticles for miR-34a delivery: biocompatibility, the potential for co-delivery of therapeutic agents, and the ability to achieve controlled drug release. Moreover, PLGA cores are biodegradable, addressing concerns about the long-term presence of non-biodegradable materials in the body[28]. This delivery results in gene regulation, inhibition of cell proliferation, and induction of cell cycle arrest, demonstrating the potential therapeutic impact of this approach.

Chitosan-modified PLGA nanoparticles are investigated as an alternative drug delivery system to improve the mentioned features[40,35]. These nanoparticles were found to improve drug release profiles and enhance cellular uptake and effectively formed complexes with miRNA, indicating their potential for gene regulation in cancer therapy.

In summary, it is presented the development of nanoparticles with biodegradable cores, primarily PLGA, for the targeted delivery of miR-34a and other therapeutic agents and after the addition of chitosan to combine their advantages and potential limitations[70,10].

2.4.2. CHITOSAN / HA

Chitosan is widely employed as a polymer in nanoparticles for drug delivery systems, both passive and active. Active targeting involves the use of ligands with specific affinities for certain receptors to enhance drug effectiveness. Nanoparticles are coated with ligands to facilitate cellular absorption through receptor-mediated endocytosis, leading to increased drug accumulation in cancer cells. Hyaluronic acid (HA) is a commonly used polysaccharide ligand for active targeting due to its high selectivity and affinity for CD44 receptors, which are overexpressed in various tumour cells.

Chitosan-hyaluronic acid nanoparticles (CHA-Np) combine the natural polysaccharides chitosan and hyaluronic acid as ligands. Their opposite charges simplify the formulation of nanoparticles, relying on electrostatic interactions between chitosan's positive charge and hyaluronic acid's negative charge[54]. CHA-Np provides controlled drug release with pH-responsive behavior, particularly in the acidic environment of cancer cells, owing to the protonation of chitosan's amide group. Additionally, the presence of hyaluronic acid

ligands enables active targeting, enhancing the accumulation of nanoparticles in tumour cells expressing CD44 receptors.

CHA-Np has found extensive application in delivering cancer therapeutics to various solid tumour types, including brain tumors, breast cancer, lung cancer, liver cancer, and colon cancer. Nevertheless, the level of CD44 receptor expression varies among different cell types, prompting researchers to collect and evaluate existing evidence to elucidate the significance and efficacy of CHA-Np in diverse cancer cells[7].

3. AIM AND OBJECTIVES

The primary objective of this project is to develop an innovative approach to design and produce co-delivery systems for drugs, with the aim of improving the effectiveness of poorly soluble drugs used in treating osteosarcoma. The central concept involves the nanoscale functionalization of miR-34a and DOX through Layer-by-Layer (LbL) assembly. This process creates a multi-layered coating to encapsulate the drug payload, facilitating targeted drug delivery.

To achieve this, the following steps will be taken:

1. The physical and chemical properties of the LbL-NPs produced will be characterized using techniques such as dynamic light scattering (DLS), Fourier-transform infrared spectroscopy - attenuated total reflectance (FTIR-ATR), X-ray photoelectron spectroscopy (XPS), and transmission electron microscopy (TEM).

2. In vitro assessments of the Novel Targeted Drug Delivery System (NTDDS) for osteosarcoma treatment will be conducted, including drug release studies and cytocompatibility tests using U2OS and SaoS-2 cell lines.

3.1. SPECIFIC OBJECTIVES

• Functionalize PLGA-CS NPs containing miR-34a and DOX and carry out Layer-by-Layer (LbL) assembly.
• Analyse the characteristics of the manufactured LbL-NPs through FTIR-ATR, XPS, DLS, QCM-D and TEM analyses.
• Use UV-Vis spectroscopy to evaluate the capability of PLGA-CS polyplexes in encapsulating and releasing miR-34a and DOX under physiological conditions.
• Determine the ideal density of U2OS and SaoS-2 spheroids to create a 3D cell model.
• Evaluate the LbL-NPs produced as a drug delivery system for osteosarcoma treatment by conducting in vitro cytocompatibility assessments, including PrestoBlue and Live/dead assays, using 2D cell models of U2OS and SaoS-2.

3.2. HYPOTHESIS

- The cytotoxicity of LbL-NPs incorporating pectin/curcumin and chitosan layers is expected to be higher in U2OS cell lines when compared to LbL-NPs with pectin and chitosan layers alone. This effect can be attributed to the anti-inflammatory and antioxidant properties of curcumin, in addition to the benefits of the triple combination therapy.

- LbL-NPs featuring an outer layer of hyaluronic acid (HA) are anticipated to exhibit increased accumulation in osteosarcoma cells in contrast to those lacking HA. This improvement in accumulation is attributed to the utilization of both active and passive targeting strategies.

4. MATERIALS AND METHODS

4.1. NPs PREPARATION

Nanoparticles containing a miRNA-34 core were synthesized using a nano-complexation method following procedures optimized in literature[10]. Here there are the steps involved in the preparation of the nanoparticles (Figure 14).

In the first step, 60mg of PLGA was introduced into a beaker containing 20ml of acetone at room temperature. Magnetic stirring was employed, aided by an IKATMC-MAG MS 7 Magnetic Stirrer, within a fume cupboard to expedite PLGA dissolution, which took approximately 30 minutes.

In a separate process, 3mg of chitosan was added to 50ml of acetic acid (0.5% v/v), along with 0.5g of Pluronic F-127 (1% w/v). This second solution was then filtered using a 0.22 µm polyamide filter to eliminate any chitosan aggregates.

Subsequently, 50µl of miRNA was added to 600 µl of the chitosan solution. This mixture was homogenized at 24,000rpm (notch 7) for 75 seconds to reduce particle size.

The two prepared solutions were then combined, with 200µl of the PLGA-containing solution being added to 650µl of the second solution (chitosan + miRNA). Mechanical stirring at 600rpm was maintained for 3 hours to facilitate solvent evaporation.

After preparation, the samples were centrifuged at 13,000rpm using a Thermo ScientificTM PicoTM 17 Microcentrifuge for 1 hour to separate the nanoparticles from the remaining liquid.

Once the optimal parameters for miRNA-containing nanoparticles were established, it was decided to incorporate anti-cancer drugs into the core to achieve multiple anti-cancer effects. This led to the creation of miRNA-Doxorubicin nanoparticles (miRDx-NPs) using the following procedure:

A 10mM doxorubicin solution was prepared in DMSO:PBS at a 1:1 ratio. Specifically, 5.4mg of doxorubicin was weighed and combined with 500ml of DMSO and 500ml of PBS in a 1.5ml Eppendorf tube. The tube was vortexed to ensure proper mixing and drug dissolution.

During the nanoparticle preparation, 2µl of the doxorubicin solution was introduced at the same time as the 50µl of miRNA, resulting in the formation of miRNA-Doxorubicin nanoparticles (miRDx-NPs).

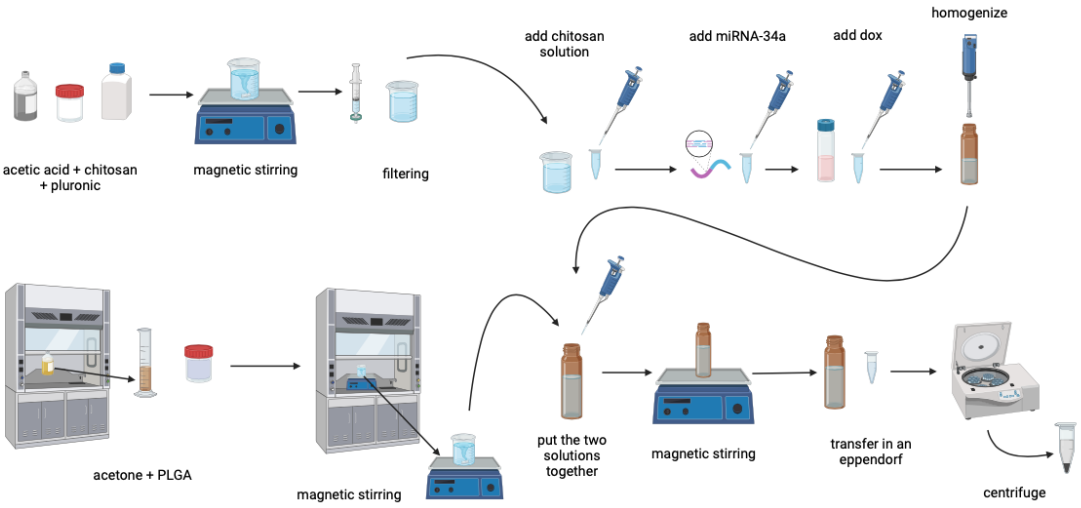

Figure 14: Polyplexes preparation, image created using Biorender

4.2. LAYER BY LAYER FORMULATION

The preparation of PLGA-CS polyplexes for Layer-by-Layer (LbL) assembly involved the following steps (Figure 15).

First, the polyplexes underwent centrifugation at 13,300rpm for 10 minutes using an AccuSpin Micro 17 centrifuge from Fisher Scientific. This step was performed to remove the supernatant.

Following centrifugation, 2ml of an electrolyte solution was cautiously added to an Eppendorf tube containing the pellet. It was gently pipetted to disperse the pellets. The purpose of this step is elaborated in Table 2.

The Eppendorf tube, now holding the pellet and electrolyte solution, was placed on a Mini Orbital Shaker (Stuart) and shaken at 93rpm for 10 minutes. This shaking action was crucial for ensuring the uniform arrangement of layers around the positively charged PLGA-CS polyplex, facilitating the entrapment of miR-34a and DOX.

Subsequently, the Eppendorf tube underwent another round of centrifugation at 13,300rpm for 10 minutes, resulting in the removal of the supernatant. This step aimed to collect the negatively charged pellet.

To eliminate any non-electrostatically attached residues, the Eppendorf tube was washed with a 1.5ml distilled water (dH2O) pH 6 buffer solution. It was then shaken for a shorter duration. Following this, the Eppendorf tube was centrifuged at 13,300rpm for 5 minutes, and the supernatant was removed to collect the negative pellet.

This entire process, from centrifugation to washing, was repeated for each layer of each type of LbL-NP, ensuring the proper construction of the multi-layered nanoparticles.

Table 1 displays the reagents and instruments used in the preparation of the electrolyte solution for each biomaterial.

Table 1: Composition of all the electrolytes used during LBL

Electrolyte solution	Reagents, brands, amounts
1mg/ml chitosan	50mg chitosan (Sigma-Aldrich) - 250µl acetic acid (Merck) - 49.75ml deionized water
2mg/ml chitosan	- 100mg chitosan (Sigma-Aldrich) - 250µl acetic acid (Merck) - 49.75ml deionized water
1mg/ml pectin	- 50mg pectin (Sigma-Aldrich) - 50ml deionised water
1mg/ml pectin/curcumin	- 50mg pectin (Sigma-Aldrich) - 50mg curcumin (Sigma-Aldrich) - 50ml deionised water
1mg/ml hyaluronic acid	- 50mg hyaluronic acid (Sigma-Aldrich) - 50ml deionised water

Table 2: Composition of the four different samples

Type of LBL	**Layer 1**	**Layer 2**	**Layer 3**	**Layer 4**	**Layer 5**
Pectin 4	1mg/ml Pectin	1mg/ml Chitosan	1mg/ml Pectin	2mg/ml Chitosan	N/A

Pectin 5	1mg/ml Pectin	1mg/ml Chitosan	1mg/ml Pectin	2mg/ml Chitosan	1mg/ml Hyaluronic Acid
Pectin – Curcumin 4	1mg/ml Pectin/Curcumin	1mg/ml Chitosan	1mg/ml Pectin/Curcumin	2mg/ml Chitosan	N/A
Pectin – Curcumin 5	1mg/ml Pectin/Curcumin	1mg/ml Chitosan	1mg/ml Pectin/Curcumin	2mg/ml Chitosan	1mg/ml Hyaluronic Acid

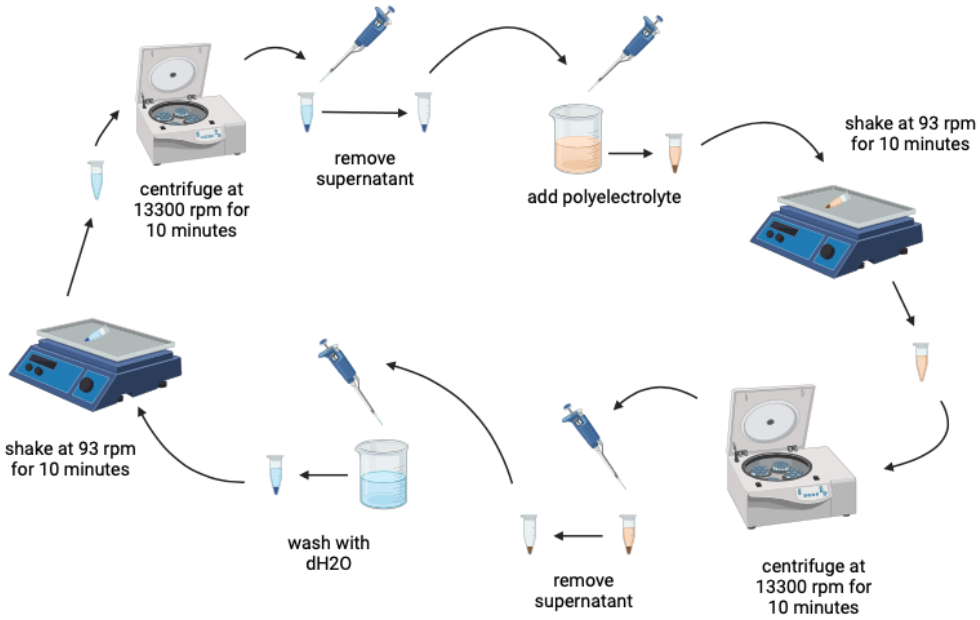

Figure 15: LBL preparation steps, image created using Biorender

4.3. PYSICOCHEMICAL CHARACTERIZATION OF LAYERS

4.3.1. DYNAMIC LIGHT SCATTERING (DLS)

Following the completion of each layer, the final pellet was carefully dispersed by gently pipetting the samples. Then, it was diluted in distilled water (dH2O) to achieve a concentration of 0.1% w/v. Subsequently, the diluted sample was pipetted into a cuvette. These cuvettes were equipped with two gold electrodes used to measure the zeta potential by applying an electrical charge between these two electrodes.

In the zeta potential measurement process, a laser beam was directed through the sample, and the instrument measured the intensity of scattered light as the particles within the sample moved through the medium. This scattering of light allowed the instrument to determine the frequency equivalent to the velocity of the particles, which, in turn, helped calculate the voltage. Multiple voltages were applied during the measurement process to accurately determine the zeta potential.

The final zeta potential value was calculated as an average of three measurements, with each measurement being obtained after a maximum of 100 runs. This measurement process was carried out using a Zetasizer Nano ZS Instrument from Malvern Panalytical Ltd.

4.3.2. FTIR-ATR

FTIR-ATR spectroscopy (Figure 16) was employed to analyze the manufactured LbL-NP samples. This analysis was conducted using a Spectrum Two PE instrument equipped with a horizontal attenuated total reflectance crystal made of ZnSe, and the instrument was provided by PerkinElmer Inc., USA.

To prepare the LbL-NP samples for FTIR analysis, the following steps were followed.

The samples were first dried in an oven at 37°C for a duration of 24 hours prior to analysis. This drying process ensured that the samples were in a suitable state for FTIR analysis.

The FTIR analysis covered a spectral range from 4000 to 550 cm^-1, allowing for the examination of a wide range of molecular vibrations and interactions within the samples. The analysis was conducted with a resolution of 2 cm^-1, ensuring detailed spectral information could be obtained for precise characterization.

This FTIR-ATR spectroscopy approach was employed to investigate the molecular composition and structure of the LbL-NPs, providing valuable insights into their chemical properties and interactions.

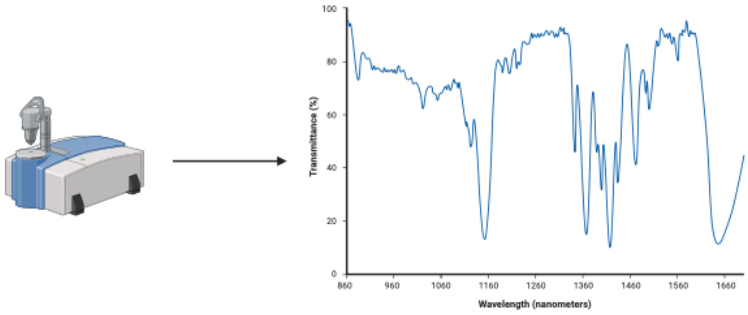

Figure 16: Example of FTIR technology, image created using Biorender

4.3.3. XPS

The XPS (X-ray Photoelectron Spectroscopy) analysis of the manufactured PLGA-CS polyplexes and LbL-NPs was carried out using a Kratos Axis UltraDLD XPS spectrometer with a scanning microprobe, equipped with a monochromatic AlKα X-ray radiation source.

Before analysis, all samples were thoroughly freeze-dried to remove moisture and ensure their stability. These prepared samples were then stored in Eppendorf tubes.

The XPS analysis was conducted at an XPS facility, specifically the EPSRC Harwell XPS Service located in Cardiff, UK.

The spectrometer used a monochromatic AlKα X-ray radiation source to irradiate the samples.

The initial analysis involved performing a survey scan to determine the atomic percentage (At%) of the elements present within the samples. This step provided an overview of the elemental composition.

CasaXPS software was employed to analyze the survey scan data and detect the binding energy (BE), which represents the chemical binding states of each element within the films.

The XPS spectra obtained for the chemical elements present in the films were subjected to peak deconvolution using the same CasaXPS software. This process helped in resolving the individual peaks and obtaining detailed information about the chemical states and bonding configurations of the elements.

XPS analysis is a powerful technique for characterizing the surface chemistry and composition of materials, providing valuable insights into the chemical properties of PLGA-CS polyplexes and LbL-NPs.

4.3.4. TEM

The size and shape of the LbL-NPs (Layer-by-Layer nanoparticles) were determined through Transmission Electron Microscopy (TEM) using a Phillips CM 100 compustage transmission electron microscope. Here are the details of the TEM analysis:

Voltage Setting: TEM imaging was conducted at a high voltage (HV) of 100.0 kV, which is a typical setting for many TEM instruments.

Magnification: Digital images were captured using an AMT CCD camera with a magnification range of 130,000x. This high level of magnification allowed for detailed visualization of the nanoparticles.

Sample Preparation: LbL-NP samples were prepared for TEM analysis by drop-casting 10µL of aqueous solutions containing the nanoparticles onto copper grids, specifically Scientific Agar grids. After drop-casting, the samples were allowed to air dry for approximately 20 seconds before capturing the TEM images.

TEM is a powerful microscopy technique that provides high-resolution images, allowing for the visualization of nanoparticles at the nanoscale, which is crucial for characterizing their size and shape accurately.

4.3.5. QCM-D

The investigation of the interaction between different layers was conducted using QCM-D analysis[19,49]. This characterization process encompassed plasma functionalization, treatment of sensors, and QCM-D experimentation.

For plasma functionalization:

The process involved aptes polymerization to introduce amino groups (negative charge) on the surface.
A bubbler was utilized to vaporize aptes, transforming it from a liquid to a vapor state.
High-pressure gas was employed to create aptes vapors, with plasma facilitating aptes polymerization.
The machine setup featured a central channel for argon and a second channel for vapor monomers, commonly used for functionalizing gold sensors in QCM-D experiments.
Operational parameters included aptes flow (2 L/min), discharge voltage (10 KV), argon flow (7.7 L/min), nitrogen flow (8 L/min), and power (20 W). Nitrogen served as the cooling gas during the process.
Plasma functionalization could be conducted in either a continuous or pulsatile mode, depending on specific requirements.

For the treatment of sensors:

The process began with a 20-second etching step without polymer to enhance surface hydrophilicity and prepare it for radical activation during polymerization.
Subsequently, a 1-minute pulsatile treatment with aptes was carried out for polymerization.
Cleaning followed the treatment, using compressed air with ethanol to remove excess aptes and prevent crystallization.

Regarding QCM-D analysis:

Quartz crystal was utilized, relying on its piezoelectric properties for this technique.
Changes in the properties of the functionalized surface led to shifts in resonance frequency.
The experiment involved introducing 300 uL of solution for each electrolyte and buffer into the QCM-D setup.

Harmonics were examined, with the first harmonic representing resonance frequency, and other odd harmonics were multiples of the first.

A baseline was established with two minutes of air exposure.

The most influenced harmonics (f1 and f13) were eliminated, and preference was given to working with f5/f7/f9 harmonics.

The QCM-D experiment concluded with a wash, displaying the actual deposited mass on the sensor.

Data was acquired throughout the experiment.

The sensor was washed with detergent at 40°C, and a gap in the graph during the washing step indicated correct material linkage and effective removal of unbound material.

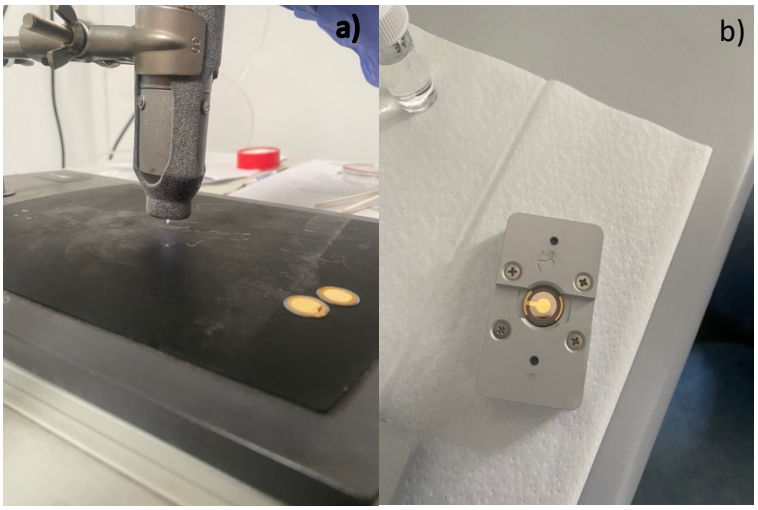

Figure 17: a) treatment of sensors; b) QCM-D technology

4.4. ENCAPSULATION EFFICENCY

4.4.1. MIRNA

To determine the encapsulation efficiency (EE) of miR-34a, the QuantiFluor® assay (Figure 18) was employed[77]. This assay utilizes a fluorescent RNA-binding dye, enabling the sensitive quantitation of small RNA amounts in purified samples. The procedure involved using an ultraviolet-visible (UV-Vis) spectrofluorometer to measure the fluorescence value generated by the RNA-binding dye.

The steps taken in accordance with the QuantiFluor® RNA system's quick protocol for a multiwell plate were as follows:

1. Preparation of Working Solution and Standard Curve: The low-concentration working solution and a standard were prepared as per the protocol.

2. Plate Preparation: A black 96-well plate was prepared for the analysis.

3. Incubation: The prepared plate was incubated at room temperature for 5 minutes, with protection from light.

4. Fluorescence Measurement: After incubation, the plate was subjected to fluorescence measurement at 492nmEx (excitation wavelength) and 540nmEm (emission wavelength). This measurement was performed using a FLUOstar Omega spectrofluorometer from DMG Labtech in Germany.

The fluorescence values obtained through this process allowed for the quantification of miR-34a. By analyzing the supernatant, the encapsulation efficiency of miR-34a in the nanoparticles could be accurately determined. Each sample was read in triplicate and referred to the standard curve generated using the standard RNA concentration.
The encapsulation efficiency (EE) was calculated using Equation 1 as follows:

$$EE(\%) = \left[\frac{(A - B)}{A}\right] * 100$$

In this equation:
- EE(%) represents the encapsulation efficiency as a percentage.
- A represents the total amount (in µg) of miR-34a that was initially added or entered into the system.
- B represents the weight (in µg) of the unencapsulated miR-34a that was recovered from the supernatant after centrifugation.

By using this formula and the data obtained from the QuantiFluor® assay, you can calculate the encapsulation efficiency, which quantifies the percentage of miR-34a that was successfully encapsulated within the nanoparticles.

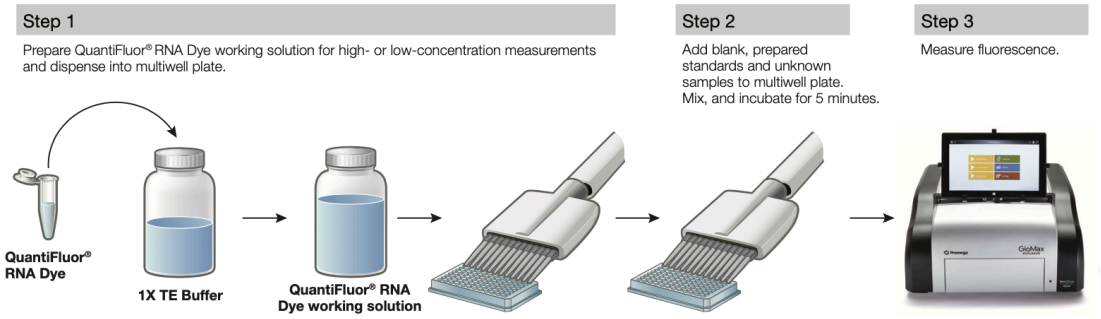

Figure 18: Quantiflour assay

4.4.2. DOX

To determine the encapsulation efficiency (EE) of DOX within the polyplex cores, an indirect measurement method was employed based on quantifying unencapsulated DOX present in the supernatant after centrifugation.

After centrifugation, supernatants containing unencapsulated DOX were collected from the samples.

The amount of unencapsulated DOX in the supernatant was determined using a UV-Vis spectrofluorometer by measuring its absorbance. This measurement was conducted at a wavelength of 480nm, specifically to detect DOX. The instrument used for this purpose was the FLUOstar Omega from DMG Labtech in Germany.

For each sample, triplicate measurements were taken, and the fluorescence values obtained were compared to a standard curve generated using free DOX at known concentrations. This standard curve served as a reference for quantification.

To ensure accurate quantification, the fluorescence values were corrected by subtracting the fluorescence values obtained from the supernatant of the polyplex without DOX (blank). This baseline correction helped account for any background fluorescence.

The encapsulation efficiency (EE) of DOX was calculated using Equation 1, similar to the method used for miR-34a encapsulation. This formula allowed for the determination of the percentage of DOX that was successfully encapsulated within the polyplex cores.

4.5. DRUG RELEASE

The evaluation of drug release, specifically miR-34a and DOX, was conducted using UV/Vis spectroscopy. The release study involved multiple steps.

Firstly, each sample, comprising manufactured nanoparticles (NPs), was prepared as described before. Subsequently, the final pellet of each sample was dispersed in 1 mL of sterile PBS (pH 7.4) to create a suitable environment for drug release.

The samples were stored in an oven at 37°C, and the release analysis was conducted at various time points, including 10 minutes, 30 minutes, 60 minutes, 2 hours, 4 hours, 7 hours, 24 hours, 48 hours, 72 hours, 96 hours, and 192 hours. This allowed for a comprehensive understanding of drug release kinetics.

At each time point, 120 µL of each sample was pipetted into a Corning Costar 96-well multi-plate. To maintain a consistent volume, 120 µL of sterile PBS was pipetted into the original samples to replace the solution that was removed. The samples were then returned to the 37°C oven until the next time point.

After all time points were completed, the microplate wells were analyzed for miR-34a release using the QuantiFluor® Assay, which measured absorbance. For the analysis of DOX release, absorbance was measured at 480nm using a FLUOstar Omega spectrofluorometer from DMG Labtech in Germany.

Standard curves were previously generated using known concentrations of miR-34a and DOX. These standard curves served as references for quantifying the concentration (in ng/well) of released miR-34a and DOX.

The cumulative release was calculated for each type of nanoparticle by adding the release values from each time point to the previous ones. This cumulative release information provides insights into the overall drug release behavior over time.

4.6. CELLS CULTURE

The human osteosarcoma cell lines SaoS-2 and U2OS were obtained from Sigma-Aldrich and cultured under specific conditions. These cells were maintained in Dulbecco's Modified Eagle's Medium (DMEM) with high glucose (Gibco, 10313-021), supplemented with 10% Fetal Bovine Serum and antibiotics (100 U/mL penicillin and 100 µg/mL streptomycin). The cultures were maintained in a controlled environment at 37°C with 5% carbon dioxide (CO2).

The cell culture process involved seeding the cells in 75cm^2 flasks, and sub-culturing was performed when the cells reached a confluence level of 70-80%. These conditions were carefully maintained to ensure the optimal growth and propagation of the cells for experimental use.

4.7. SPHEROIDS PREPARATION AND CHARACTERIZATION

Spheroids of SaoS-2 and U2OS cells were generated using a modified low-attachment technique. The process began with the preparation of a 0.25% Methylcellulose medium in DMEM with high glucose, which was done at least 24 hours prior to spheroid formation.

To initiate spheroid formation, cells were seeded in a Costar UltraLow Attachment 96-well plate at different densities, such as 50,000 (50K) and 100,000 (100K) cells per well, in the 0.25% Methylcellulose DMEM. This step followed the previous culture of cells in a flask until they reached around 90% confluence. After rinsing with sterile PBS, the cells were detached using trypsin and counted. The cell suspension was adjusted to achieve the desired cell densities.

The calculation of the total number of cells to be retained after the centrifugation step was performed using equation2.

$$n°cells = n°well * cell\ density\ needed$$

Subsequently, the cell suspension was centrifuged at 1,200 rpm for 5 minutes, and the resulting cell pellet was resuspended in fresh 0.25% Methylcellulose DMEM. Vigorous pipetting was employed to encourage cell aggregation and ensure even dispersion.

In each well of the 96-well plate, 150 µL of the cell suspension, containing cells and 0.25% Methylcellulose DMEM, was added. The plate was then incubated at 37°C in an environment with 5% CO2 to facilitate spheroid formation.

During the spheroid culturing process, fresh 0.25% Methylcellulose DMEM was added every two days. The Costar UltraLow Attachment 96-well plate was cultured for a total of ten days to observe spheroid formation.

The spheroids derived from both SaoS-2 and U2OS cells were subjected to analysis at six different time points (1, 2, 3, 4, 7, and 10 days) to monitor their growth and changes over time. This analysis involved imaging the spheroids at each time point using the TRANS filter on the EVOS M5000 Fluorescence microscope. The spheroids' diameters were quantitatively analyzed at each time point using Image J software, a widely used image processing and analysis tool.

The collected data on spheroid diameter at each time point provided valuable insights into the growth and dynamics of these 3D cell models. This information was essential for various studies and experiments involving spheroid cultures, allowing researchers to track their development and assess changes in size and morphology (Figure 15).

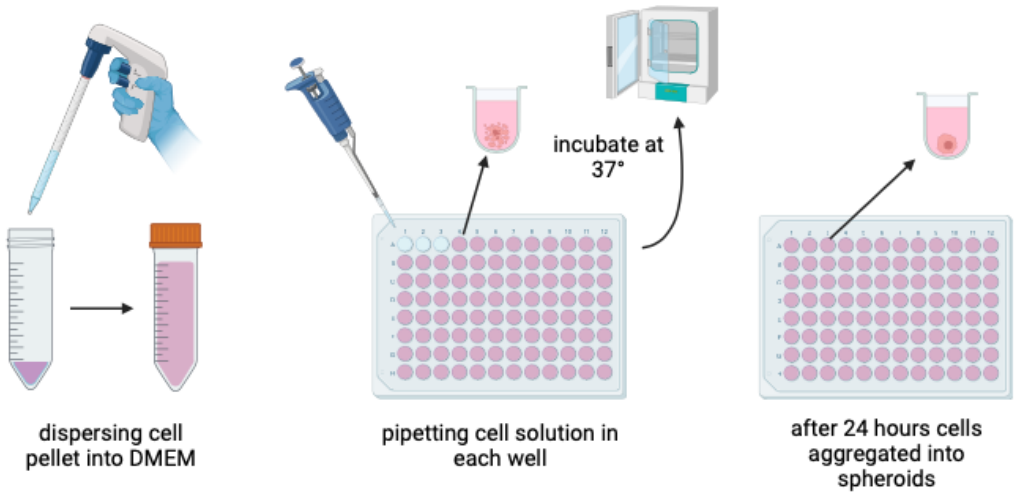

Figure 19: Preparation of spheroids starting from cell pellet, image created using Biorender

4.8. CELLS TEST

To create 2D cell models using U2OS and SaoS-2 cell cultures, we followed this procedure.

First, when the cell culture reached approximately 90% confluence in a 75cm^2 flask, we removed the Dulbecco's Modified Eagle's Medium (DMEM). Next, we washed the cells in the flask with phosphate-buffered saline (PBS). To detach the cells from the flask surface, we added 3 mL of trypsin to the flask and incubated it at 37°C for 5 minutes. After incubation, we added DMEM to the flask to reach a total volume of 10 mL. We then centrifuged the solution in the flask at 1200 rpm for 5 minutes.

For cell counting (Figure 20), following centrifugation, we carefully removed the DMEM from the cell pellets and added fresh DMEM to the cell pellets, homogenizing the mixture. To count the cells, we placed 10 µL of the cell solution on a grid glass slide and examined it under a microscope. We calculated the number of cells present in the 10 mL solution using Equation 3:

$$Number\ of\ Cells\ =\ Average\ number\ of\ cells\ counted\ \times\ 10\ \times\ 10^4$$

To prepare the cell solution for experiments, we utilized Equation 2 to determine the number of cells required. We then prepared the cell solution to achieve 8,000 cells per well by applying proportion calculations as shown in Equation 4:

$$n°cell\ required: unknown\ =\ n°cells\ in\ flask: 10\ mL$$

The calculated amount of cell solution needed to achieve the desired number of cells (8,000 cells per well) was pipetted into a separate falcon tube, and fresh DMEM was added to the cell solution to ensure that 150 µL of cell solution could be added to each well.

For cell seeding and incubation, we seeded the cell solution onto a Corning Costar 96-well multi-plate and incubated it at 37°C in a 5% CO2 environment for 24 hours before treatment with manufactured LbL-NPs.

In the treatment and analysis phase, the 2D cell models were treated with manufactured LbL-NPs, and they were further incubated at 37°C in a 5% CO2 environment for 24 hours and 5 days. Cell viability and metabolic activity were assessed at each time point using different concentrations of each type of LbL-NPs, including 100, 500, and 1000 µg/mL.
This protocol enabled the creation of 2D cell models and the evaluation of cell viability and metabolic activity following treatment with LbL-NPs at various concentrations and time points.

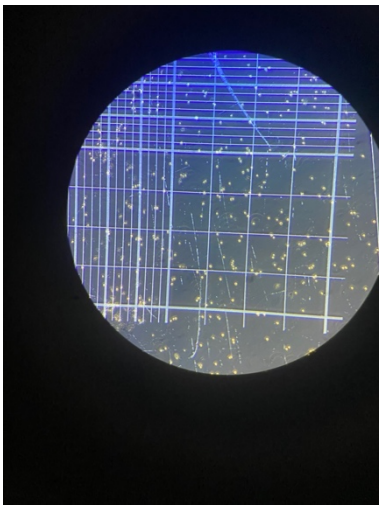

Figure 20: Cells on grid for counting

4.8.1. LIVE AND DEAD ASSAY

To assess the impact of different types and concentrations of manufactured LbL-NPs on the viability of U2OS cells, we employed the Live/Dead assay[98]. Here's a description of the procedure (Figure 21).
First, we prepared the Live/Dead staining solution by mixing 4 mL of sterile phosphate-buffered saline (PBS) with eight drops of NucBlue Live (for live cells) and Propidium Iodide (for dead cells).
Next, the 2D cell models, which had been treated with the manufactured LbL-NPs and incubated for either 24 hours or 5 days, as per our experimental setup, were used.
We washed the cell samples twice with sterile PBS after the respective incubation periods.

Then, we applied 100 µL of the prepared Live/Dead staining solution to both the LbL-NP treated samples and the cell control for each sample.

To protect them from light, we covered the Corning Costar 96-well multi-plate with foil. We incubated the plate at 37°C in a 5% CO2 environment for 20-30 minutes to allow for proper staining.

After staining, we used an EVOS M5000 fluorescence microscope from Thermo Fisher Scientific to capture images of each well. We utilized both 4',6-diamidino-2-phenylindole (DAPI) and red fluorescent protein (RFP) filters to visualize Live and Dead cells, respectively.

By following this Live/Dead assay procedure, we were able to assess the viability of U2OS cells treated with different concentrations of various LbL-NPs at two different time points (24 hours and 5 days). The fluorescent staining provided valuable insights into cell viability and allowed for the differentiation of live and dead cell populations within the samples.

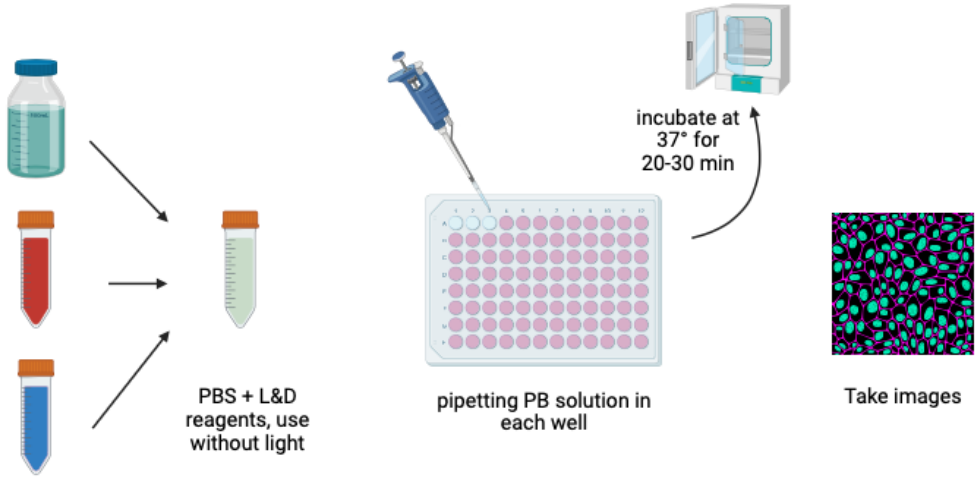

Figure 21: L&D assay protocol

4.8.2. PRESTO BLUE ASSAY

The PrestoBlue assay is a valuable technique for evaluating cell viability and metabolic activity based on the reduction power of living cells (Figure 22)[97]. To perform this assay, the PrestoBlue solution is prepared by diluting the PrestoBlue reagent in Dulbecco's Modified Eagle's Medium (DMEM) at a 1:10 ratio.

The 2D cell models, which were previously incubated at 37°C in a 5% CO2 environment for the specified time points, had their cell culture medium (DMEM) removed from each well. Then, 200 µL of the prepared PrestoBlue solution was added to each well after washing them with sterile phosphate-buffered saline (PBS). Controls, including a 10 nM DOX solution and cells without treatment, were also included.

To protect the samples from light, the multi-plate was covered with foil, and the samples were incubated for one hour. This allowed the PrestoBlue reagent to interact with the cells. After incubation, the fluorescence was measured at Ex544nm/Em590nm using appropriate fluorescence settings.

This PrestoBlue assay allows for the assessment of metabolic activity and cell viability of both SaoS-2 and U2OS cells under different experimental conditions, including exposure to different concentrations of various LbL-NPs at specific time points. The change in fluorescence provides valuable information about the health and metabolic activity of the cells in response to these conditions.

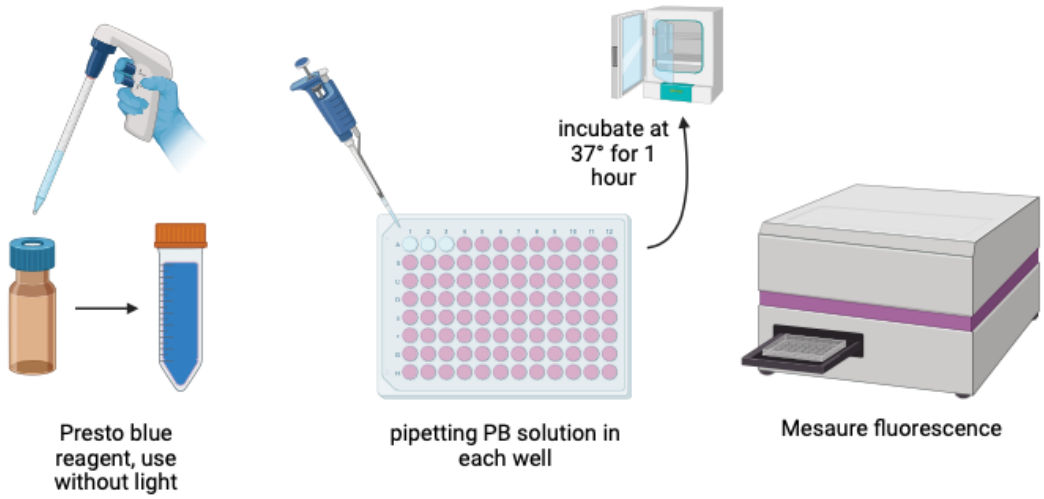

Figure 22: Presto blue protocol

5. RESULTS

5.1. PYSICOCHEMICAL CHARACTERIZATION OF LBL

5.1.1. DLS

In order to assess the electrostatic interactions within the LbL assembly layers, we conducted zeta potential measurements, following the previously outlined procedure. When comparing the P4/P5 and PC4/PC5 samples, it was observed that the 1mg/mL pectin/curcumin biomaterial in layer 3 exhibited a notably more negative zeta potential compared to the 1mg/mL pectin alone. For layer 2 in all LbL-NPs, a 1mg/mL CS solution was employed, yielding zeta potential values of -2.93 (+- 1.27) mV and -2.84 (+- 14.9) mV. Consequently, the zeta potential differences between the P4/P5 and PC4/PC5 samples were not found to be statistically significant (refer to Table 3, 4) (Figure 23, 24). To attain a positive zeta potential for layer 4 comprised of CS, we optimized and prepared an electrolyte solution containing 2mg/mL CS. For the active-targeting layer 5, a 1mg/mL HA electrolyte solution was utilized, resulting in a negative zeta potential that did not exhibit significant variations between the P5 and PC5 samples.

Table 3: Mean Zeta potential and standard deviation of each layer without curcumin

Layer Number	*P4/P5*	*Mean Zeta Potential (mV)*	*St Dev*
1	Pectin/Curcumin (1mg/mL pH6)	-38.4	2.48
2	Chitosan (1mg/mL pH6)	-2.93	1.27
3	Pectin/Curcumin (1mg/mL pH6)	-14.8	4.08
4	Chitosan (2mg/mL pH6)	11.8	3.74
5	Hyaluronic acid (1mg/mL pH6)	-9.62	2.24

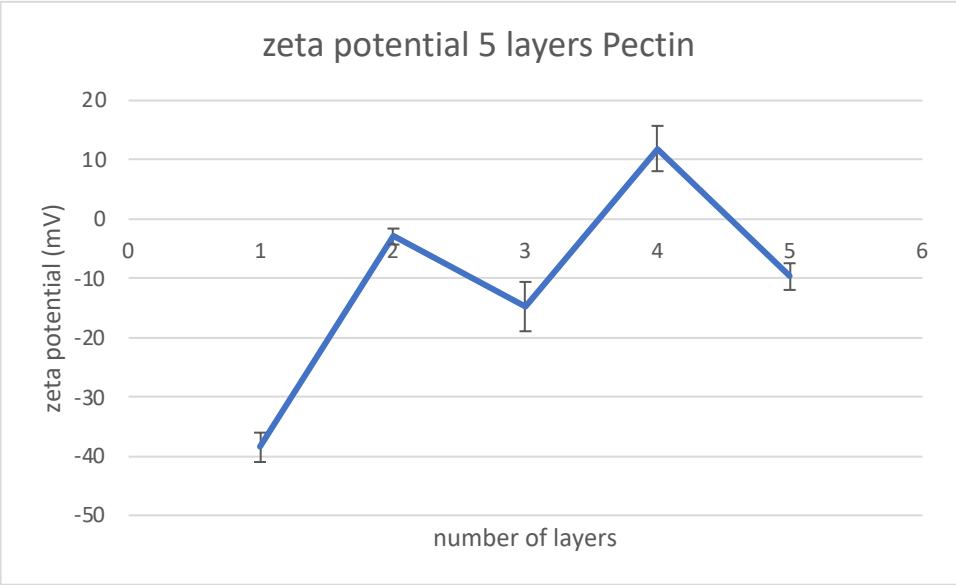

Figure 23: Zeta potential across layers without curcumin

Table 4: Mean Zeta potential and standard deviation of each layer with curcumin

Layer Number	*PC4/PC5*	*Mean Zeta Potential (mV)*	*St Dev (mV)*
1	Pectin (1mg/mL pH6)	-43.36	2.11
2	Chitosan (1mg/mL pH6)	-2.84	14.9
3	Pectin (1mg/mL pH6)	-18.63	4.36
4	Chitosan (2mg/mL pH6)	15.13	3.87
5	Hyaluronic acid (1mg/mL pH6)	-28.93	15.08

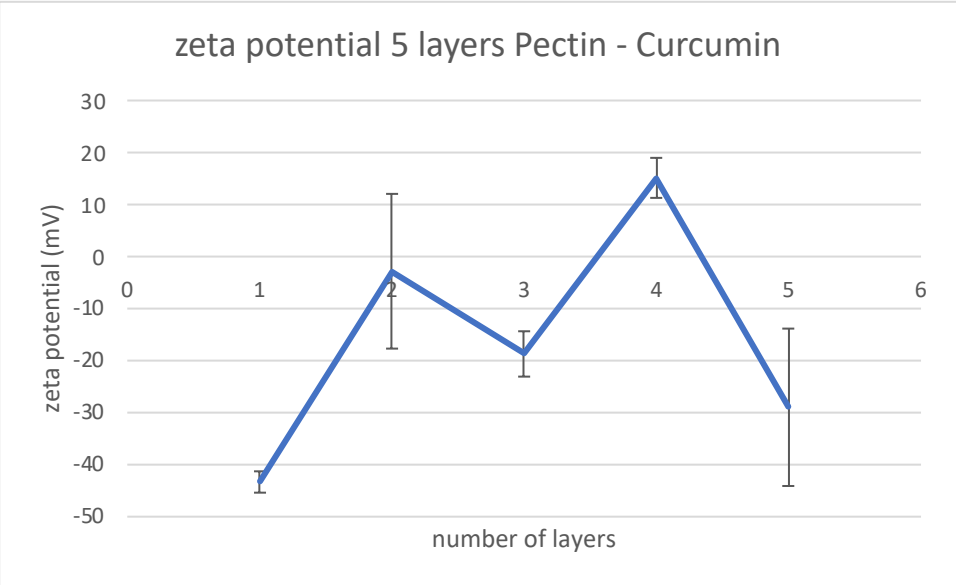

Figure 24: Zeta potential across layers without curcumin

5.1.2. FTIR

The samples were prepared using the method previously outlined. Figure 25 and Table 5 illustrate a comparison between the spectra of the manufactured PLGA-CS polyplex and LbL-NPs. Similar absorption peaks were observed at wavelengths 2250, 2700, and 2800 cm-1 in the spectra of PLGA-CS polyplex, P4, and P5. These peaks correspond to the stretching vibrations of C-O, O-H, and C-H in the CH2 groups.

In contrast, samples PC4 and PC5 exhibited absorption peaks in the ranges of 2300-2800 cm-1 and 3400-3500 cm-1, which were attributed to C-H stretching and O-H stretching. Furthermore, absorption peaks at approximately 1001 cm-1 were indicative of C-O-C bonds. Notably, N-H bond-related peaks were discernible at around 3437 cm-1 and 500 cm-1 in PC4 and PC5.

The analysis of all the manufactured NP samples was carried out across a wavelength range spanning from 4000 to 550 cm-1, utilizing a resolution of 2 cm-1. The absorbance was graphed against the respective wavelengths, and the bonds corresponding to the absorption peaks have been indicated with arrows. In the graphical representation, the miRD-NP sample is denoted in black, the P4 LbL-NP sample in pink, the P5 LbL-NP sample in green, the PC4 LbL-NP sample in blue, and the PC5 LbL-NP sample in yellow[76,78,79].

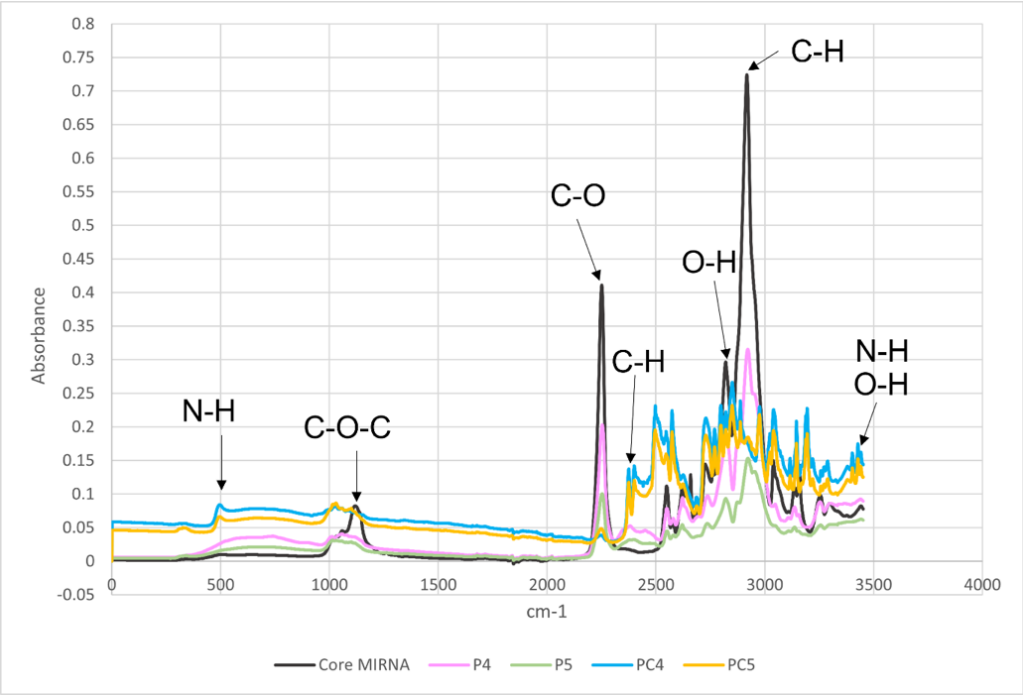

Figure 25: FTIR spectrum of NPs

Table 5: FTIR analysis of NPs

Type of NP	Wavelength (cm^1)	Bond
PLGA-CS polyplex	2250	C-O
	2700	O-H
	2800	C-H
	3100	O-H
P4	2250	C-O
	2700	O-H
	2800	C-H
P5	2250	C-O
	2700	O-H
	2800	C-H
PC4	500	C=C
	1001	C-O-C
	2300-2800	C-H
	3100	O-H

	3400-3500	O-H/N-H
PC5	500	C=C
	1001	C-O-C
	2300-2800	C-H
	3100	O-H
	3400-3500	O-H/N-H

5.1.3. XPS

The manufactured PLGA-CS polyplex, encapsulating DOX and miR-34a, as well as the LbL-NPs, underwent in-depth chemical characterization using CasaXPS software. This analysis generated an XPS survey and components of both C1s and O1s were calculated, allowing for the identification of specific chemical bonds.

In the XPS analysis of the PLGA-CS polyplex, the presence of C1s was confirmed, representing C=O and C-O bonds (doxo and chitosan presence respectively) (Figure 26) (Table 6). The dominant components of O1s were attributed to C=O bonds, accounting for 67.69%. Silicon was observed in all samples at low atomic percentages (At%), ranging from 0.89% to 6.89%.

Comparing the P5 and P4 samples, similarities were evident. The O1s XPS analysis recorded approximately 75 At% of C-O bonds. Additionally, both P4 and P5 samples exhibited the presence of nitrogen, with P5 having a slight increase in nitrogen content (0.78%) compared to P4 (Figure 27, 28) (Table 7, 8). However, differences were also observed; specifically, the P4 sample contained fluorine, while the P5 sample did not.

From the O1s and C1s XPS analysis, disparities between the PC4 and PC5 samples were evident (Figure 29) (Table 9, 10). PC5 exhibited the highest At% (65.48%) for the C=O bond in the O1s spectrum, while PC4 had the highest At% (63.68%) attributed to the C-C bond in the C1s spectrum[80,81].

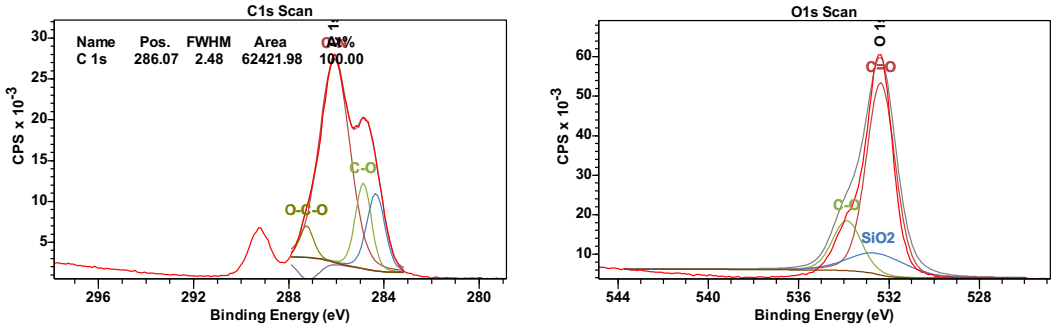

Figure 26: XPS spectrum of core (OS1, CS1)

Table 6: XPS analysis of core

Element	Bond	Position (eV)	% At Conc
C1s	C-N	286.08	65.66
C1s	C-O	284.87	14.61
C1s	C-C/C-H	284.35	14.90
C1s	C=O	287.18	0.00
C1s	O-C-O	287.26	4.87
O1s	C=O	532.37	67.69
O1s	C-O	533.87	17.55
O1s	SiO_2	532.47	14.76

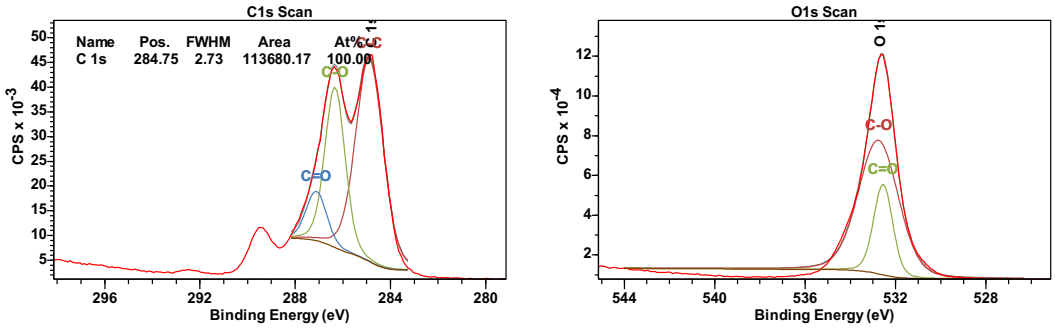

Figure 27: XPS spectrum of P4 (OS1,CS1)

Table 7: XPS analysis of P4

Element	Bond	Position (eV)	% At Conc
C1s	C-C/C-H	284.88	56.85
C1s	C-O	286.33	32.90
C1s	C=O	287.11	10.25
O1s	C=O	532.55	24.50
O1s	C-O	532.76	75.50

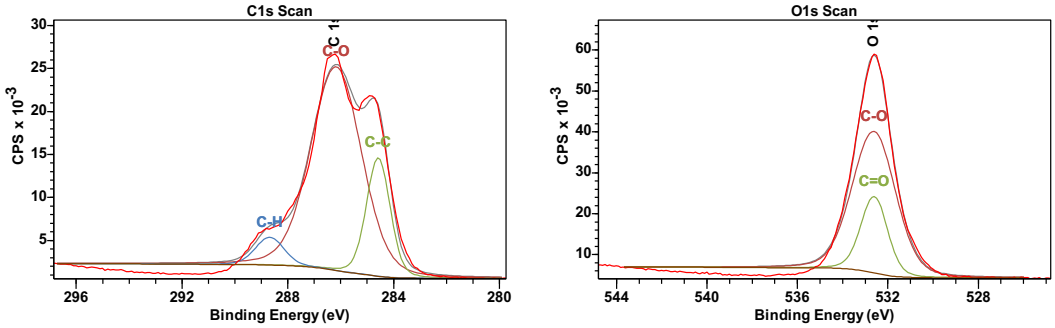

Figure 28: XPS spectrum of P5 (OS1, CS1)

Table 8: XPS analysis of P5

Element	Bond	Position (eV)	% At Conc
C1s	C-O	286.17	74.13
C1s	C-C	284.58	20.15
C1s	C=O/O-C-O	288.68	5.72
O1s	C-O	532.61	74.99
O1s	C=O	532.60	25.01

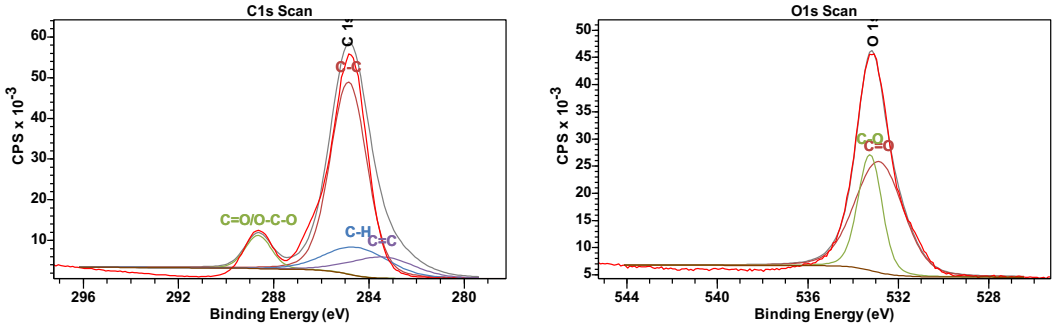

Figure 29: XPS spectrum of PC4 and PC5

Table 9: XPS analysis of PC4

Element	Bond	Position (eV)	% At Conc
C1s	C-C	284.85	63.68
C1s	C=O/O-C-O	288.65	7.97
C1s	C-H	284.45	16.19
C1s	C=C	283.45	12.17

Table 10: XPS analysis of PC5

Element	Bond	Position (eV)	% At Conc
O1s	C=O	532.85	65.48
O1s	C-O	533.26	34.16

5.1.4. TEM

The morphology of LbL-NPs was examined using TEM analysis, as illustrated in Figure 30. Subsequently, an analysis was conducted using Image J software to calculate the mean size of the nanoparticles observed in the TEM image. The results indicated that LbL-NPs P4 exhibited a mean diameter of 247.17 nm. It's important to note that the diameter sizes of the LbL-NPs varied within a range from 198.83 nm to 347 nm.

P5/pc5

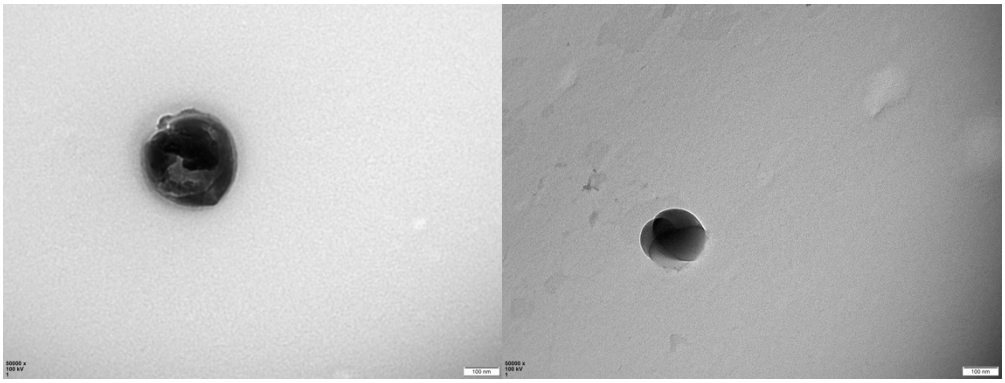

Figure 30: TEM images of P5 and PC5

5.1.5. QCM-D

The interaction between the different materials composing layers was evaluated using QCM-D.

It was analyzed separately the two formulations: the fist one was the 4 layers formulation with chitosan and pectin, the second one was the 5 layers formulation with the addition of hyaluronic acid as the last layer.

It’s preferred to chose the 7 frequency and 7 dispersion to reach a more stable measurement.

In the first formulation it is evident a little gap between the washing step and the polyelectrolyte deposition, so it means that there is a good interaction between pectin and chitosan.

In the second formulation there is the adding of hyaluronic acid as fifth layer and it is shown that it have a little influence in the interactions demonstrate by the increase of the graphic gap (Figure 31).

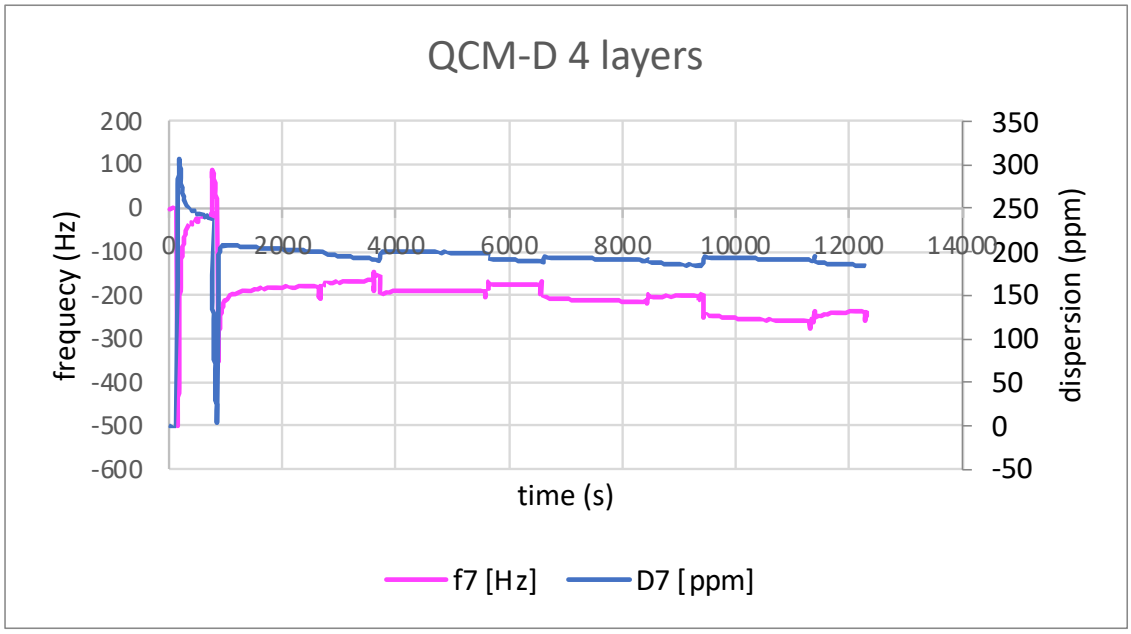

Figure 31: QCM-D spectrum of PC4

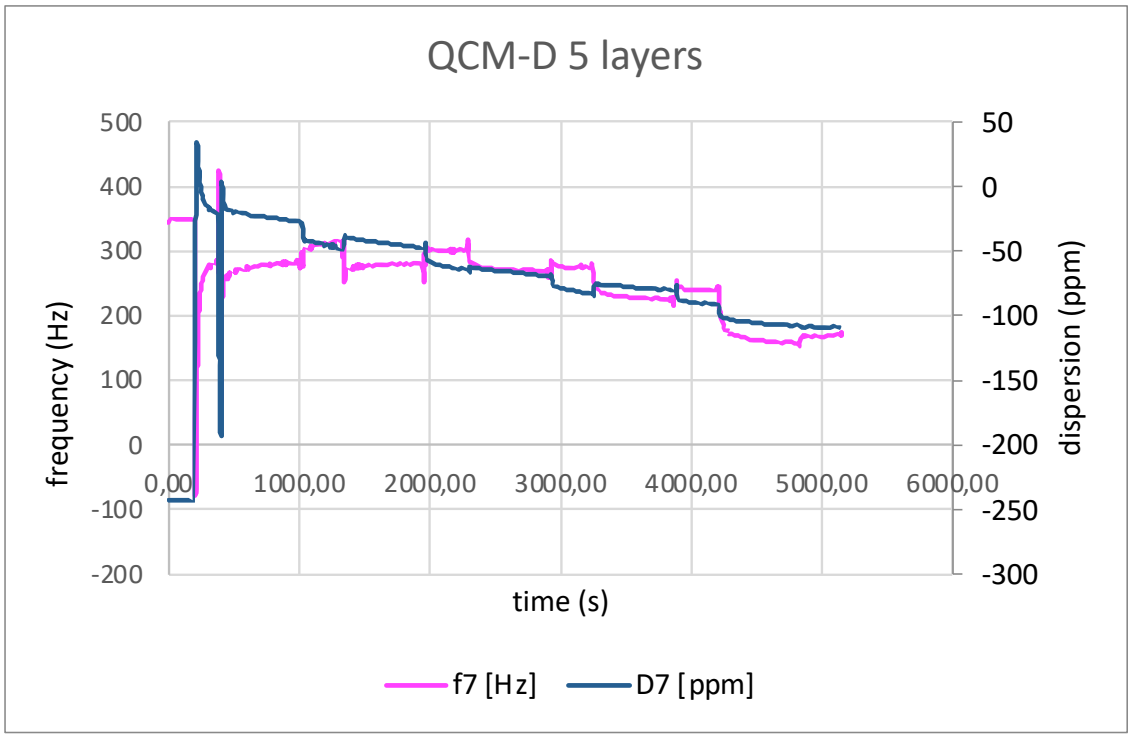

Figure 32: QCM-D spectrum of PC5

5.2. CHARACTERIZATION OF NPS

5.2.1. ENCAPSULATION EFFICENCY OF MIRNA AND DOX

The encapsulation efficiencies (EE) of PLGA-CS polyplexes containing miR-34a (miR-NPs) and PLGA-CS polyplexes containing both miR-34a and DOX (miRD-NPs) were compared and are depicted in Figure 32.

For miR-34a, a mean EE of 99.97% was calculated for both miR-NPs and miRD-NPs. Notably, there was no significant difference observed in the EE of miR-34a between miR-NPs and miRD-NPs, as indicated by a p-value of 0.117.

Furthermore, in the case of DOX, the mean EE of 69.74% was calculated for miRD-NPs. This suggests that the PLGA-CS polyplexes exhibit a notably higher encapsulation efficiency for miR-34a compared to DOX.

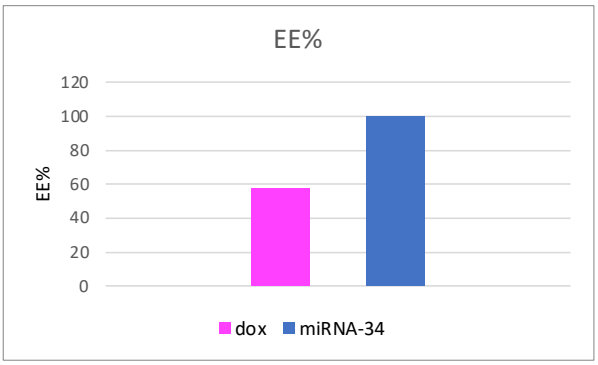

Figure 33: Encaosulation efficency of miRNA-34 and dox

5.2.2. RELASE OF MIRNA AND DOX

To assess the release profiles of miR-34a and DOX from all the manufactured nanoparticles (NPs), the NPs were incubated at 37°C in PBS at pH 7.4, mimicking conditions relevant to storage and blood plasma. The analysis of the release followed the method previously described. The comparison of the cumulative release of miR-34a and DOX from the four different types of manufactured LbL-NPs is presented in Figure 34, Figure 35.

From the 3-day to 8-day time points, it was observed that both the P4 and P5 samples had a significantly higher cumulative release of miR-34a compared to the PC4 and PC5 samples (Figure 35). In contrast, the PC4 samples displayed the lowest cumulative release of miR-34a between the 24-hour and 4-day timepoints (Figure 35).

Additionally, both the P4 and PC5 samples exhibited a significantly higher cumulative release of DOX from the 48-hour to 8-day time points compared to the P5 and PC4 samples (Figure 34). Furthermore, different trends were observed among the five LbL-NP types. Specifically, the P5 samples demonstrated a significantly lower cumulative DOX release from the 48-hour time point compared to P4, while PC5 exhibited a significantly higher cumulative DOX release from the 48-hour time point compared to PC4 (Figure 34).

A one-way ANOVA statistical test with Tukey comparison was conducted to compare the cumulative release from the last two time points (4-day and 8-day) and identify the confidence intervals and p-values for each type of LbL-NPs manufactured. This statistical test revealed that P4 and PC4 samples had a significantly different cumulative release of miR-34a between the last two time points, whereas PC5 and P5 samples did not exhibit

significant differences (P-values < 0.05). Furthermore, all the manufactured LbL-NP types did not display a significantly different cumulative release of DOX between the last two time points (P-values > 0.05) (Figure 34).

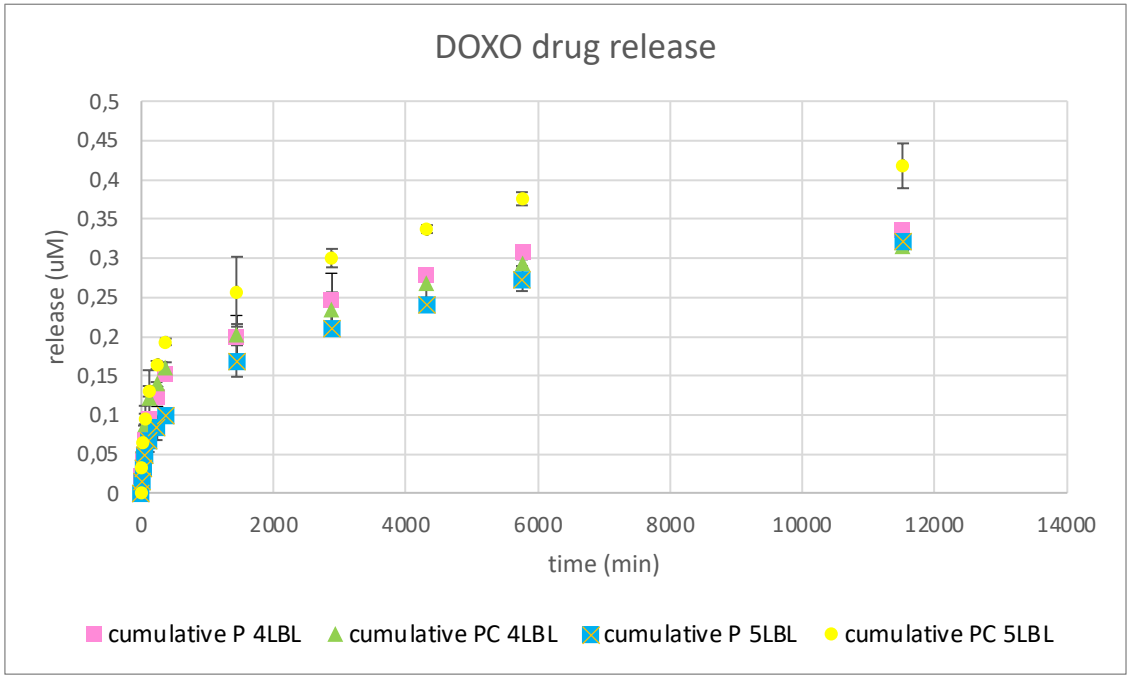

Figure 34: Release profile of dox

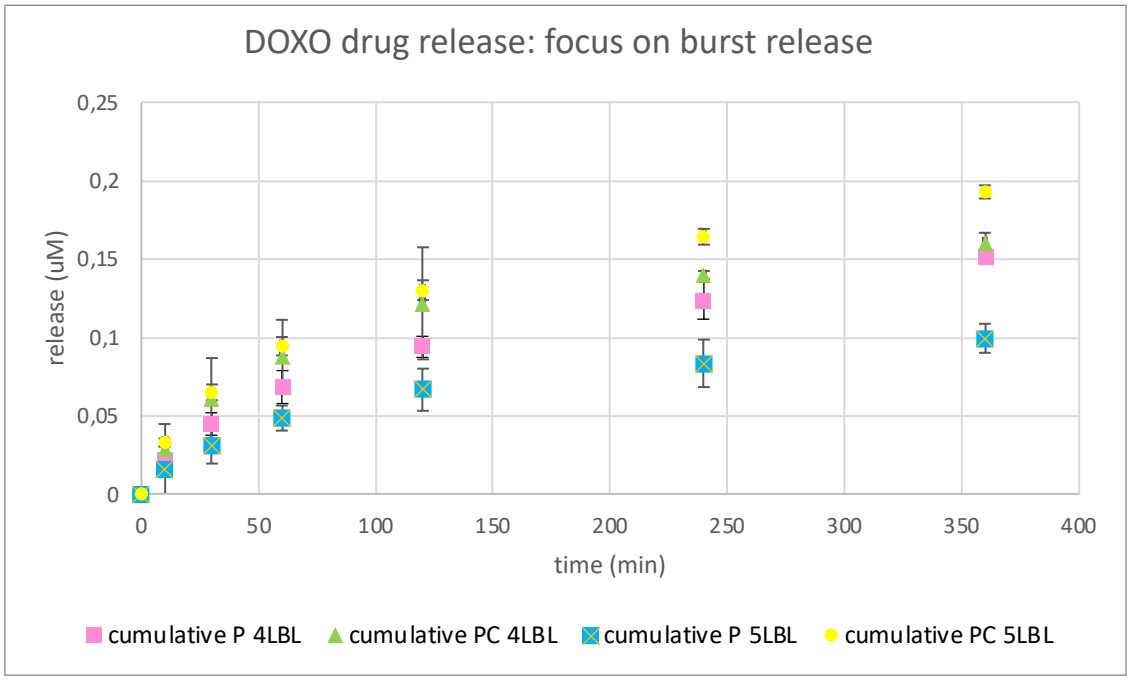

Figure 35: Release profile of dox, focus on burst release

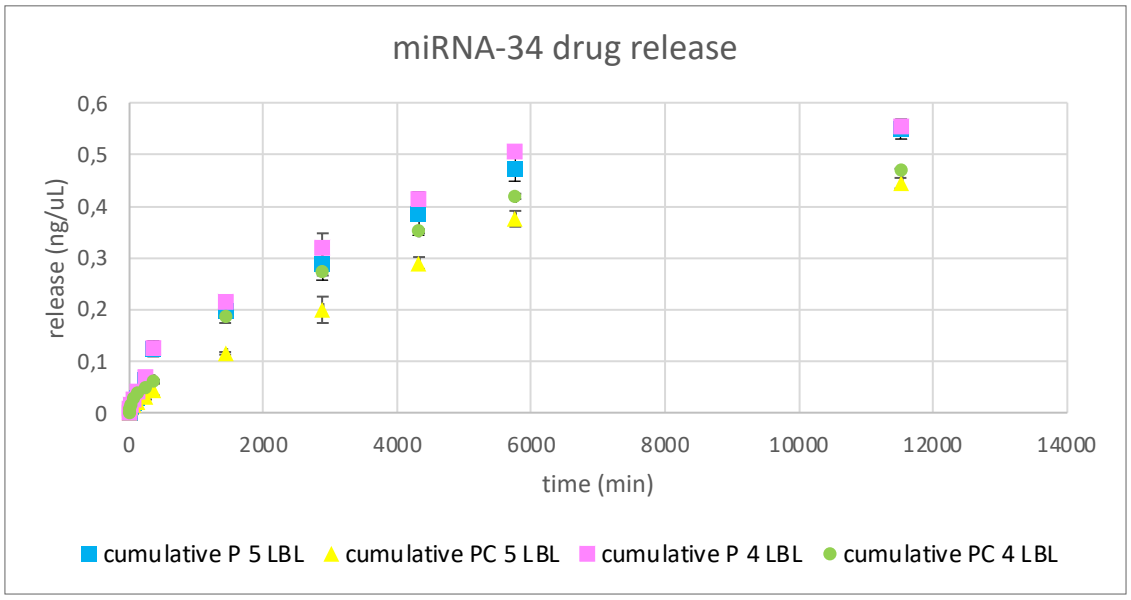

Figure 36: Release profile of miRNA-34

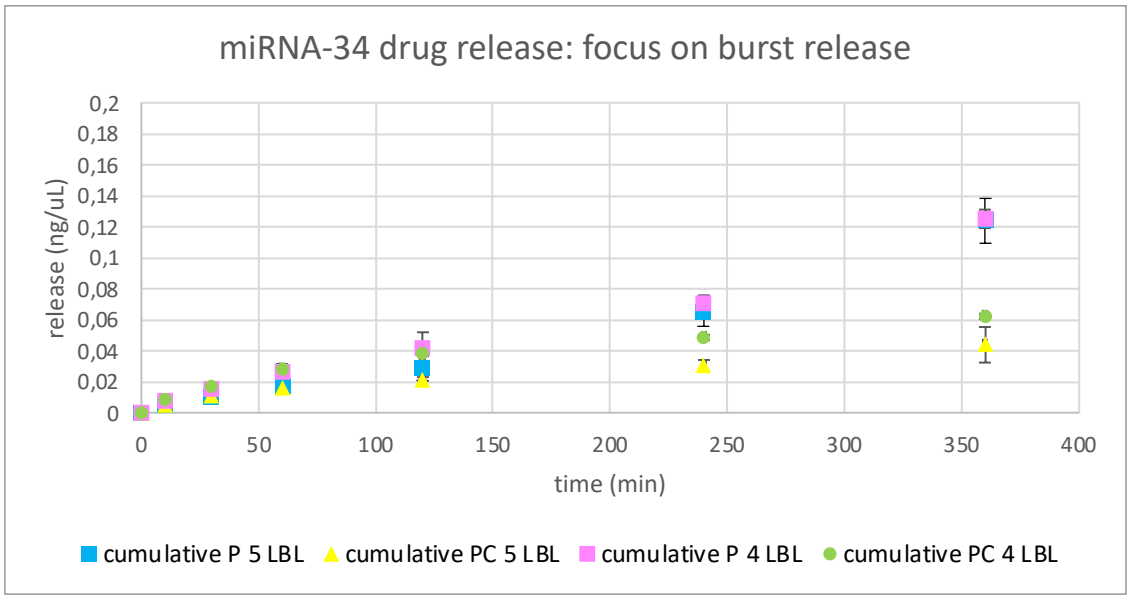

Figure 37: Release profile of miRNA-34, focus on burst release

5.3. MORPHOLOGY OF SPHEROIDS

The 3D models of U2OS and SaoS-2 cell lines were constructed using the previously described method. Figure 35, 36 provides an illustration of the spheroid morphology over a ten-day period, while the mean diameters at each time point were determined using Image J and are presented in Figure 37.

There are notable differences in the morphology of the U2OS and SaoS-2 spheroids. U2OS spheroids appear to exhibit a greater roundness and compactness, whereas SaoS-2 spheroids are less compact (Figure 35).

Additionally, the trends in spheroid growth vary between the U2OS and SaoS-2 spheroid models. In the case of SaoS-2 spheroids, they began with a mean diameter of 972.32 µm at 24 hours and gradually increased in size, reaching 2252.29 µm by ten days.

Conversely, the growth patterns of U2OS spheroids differ depending on the initial cell densities. The 50K U2OS spheroids displayed fluctuations in mean diameter between 24 and 72 hours, maintaining a relatively consistent diameter over the course of ten days. In contrast, the 100K U2OS spheroids exhibited variations in mean diameter that increased and decreased over the ten-day period.

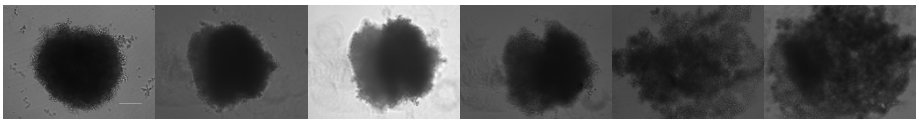

Figure 38: 50 k SAOS spheroids shape along time (24h, 48, 3d, 4d, 7d, 10d)

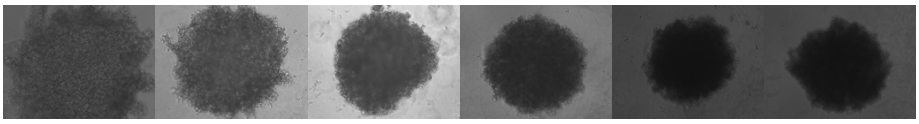

Figure 39: 20k U2OS spheroids shape along time (24h, 48, 3d, 4d, 7d, 10d)

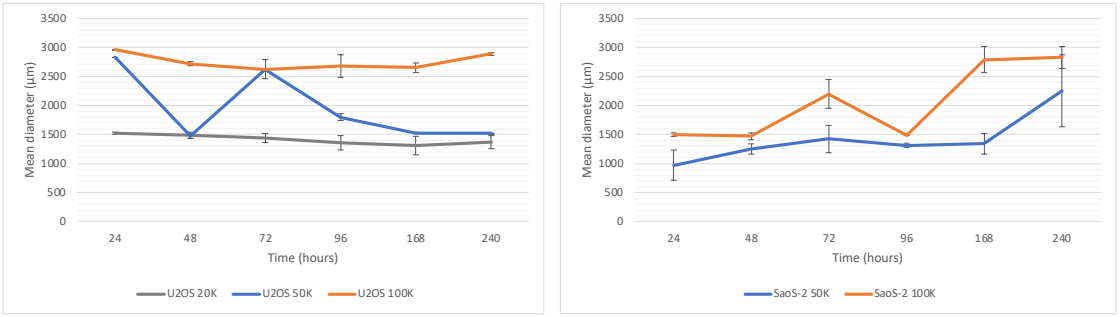

Figure 40: Mean diameter of U2OS and SAOS along time

5.4. EVALUATION OF INTERACTION BETWEEN CELL LINES AND NPS

5.4.1. LIVE AND DEAD ASSAY

Figures 38, 39 depict live (in blue) and dead (in red) U2OS cells in the 2D model, providing a visual representation of cell viability when exposed to different manufactured LbL-NPs.

The analysis is conducted at two time points, 24 hours and five days, and with varying LbL-NP concentrations, including 100, 500, and 1000 µg/ml.

When examining the cells treated with P5 and PC5 LbL-NPs for 24 hours (Figure 38), a striking observation is the notably higher level of apoptotic activity compared to cells treated with P4 and PC4 LbL-NPs. Nevertheless, it's important to note that cell death is also present in the cells treated with P4 and PC4 LbL-NPs (Figure 38).

Over the course of five days, there is a significant reduction in the number of live cells in cultures exposed to the manufactured LbL-NPs compared to the 24-hour time point (Figure 38, 39). Furthermore, as the LbL-NP concentrations increase, apoptotic activity rises over the five-day period, except in the case of cells treated with PC5 (Figure 39). Of particular note is the remarkable difference observed with LbL-NP PC5 compared to the other treatments; there is a significantly higher level of cell death in all concentrations of PC5 treatment (Figure 39).

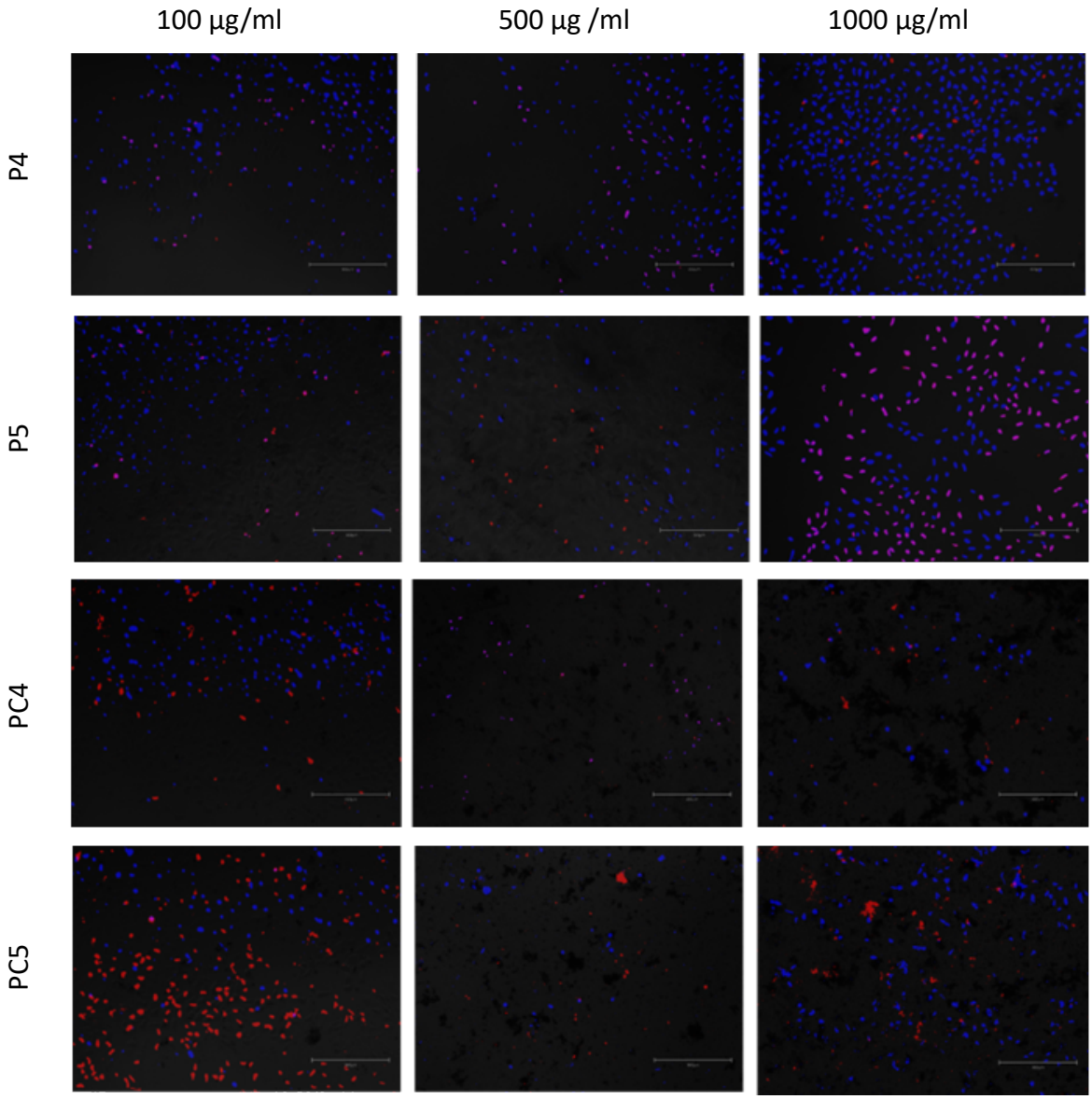

Figure 41: L&D imaging of U2OS after 24 hours

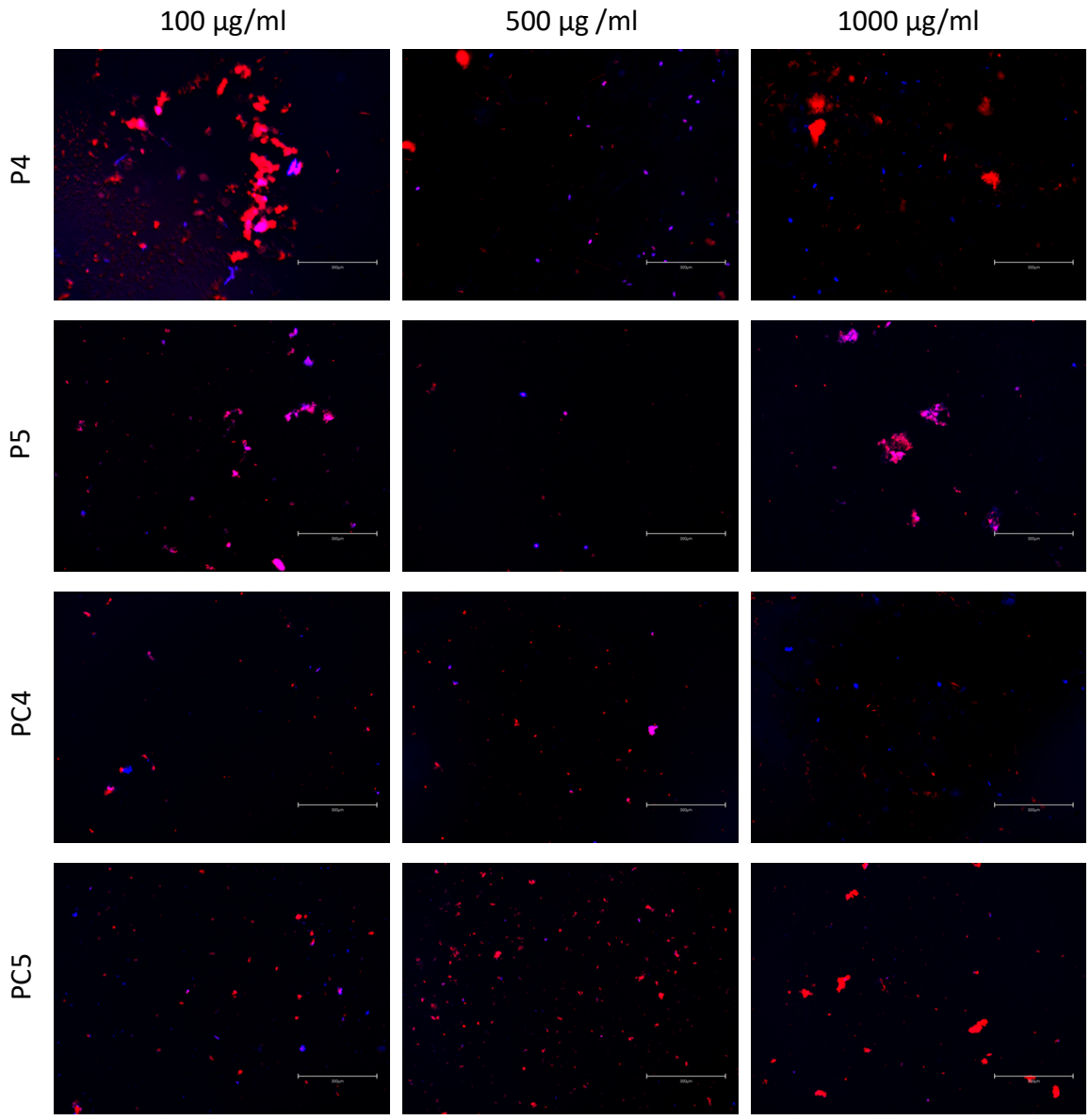

Figure 42: L&D imaging of U2OS after 5 days

5.4.2. PRESTO BLUE ASSAY

Figure 40, 41 provides an overview of the impact of different concentrations of LbL-NPs on the metabolic activity of SaoS-2 and U2OS cell models. The analysis covers two time points: 24 hours and five days.

For SaoS-2 cells treated with all the manufactured LbL-NPs for 24 hours and five days, there was no significant difference observed in metabolic activity compared to untreated cells (P-value > 0.05) (Figure 40,41). Although there is a consistent trend in the metabolic activity of SaoS-2 cells after five days of treatment with all the LbL-NPs at different NP

concentrations, it appears that PC4 and PC5 LbL-NPs may slightly reduce the metabolic activity of SaoS-2 cells compared to P4 and P5 LbL-NPs (Figure 40,41).

In contrast, the effect of LbL-NPs on the metabolic activity of U2OS cells was compared to untreated U2OS cells, as shown in Figures 40 and 41. U2OS cells treated with LbL-NPs PC4 and PC5 for 24 hours exhibited significantly lower metabolic activity compared to untreated U2OS cells (P-value < 0.05 with 100µg/ml LbL-NPs and P-value < 0.001 with 500 and 1000µg/ml LbL-NPs) (Figure 40, 41). Conversely, U2OS cells treated with LbL-NP P5 for 24 hours had significantly higher metabolic activity compared to untreated U2OS cells (P-value < 0.001 with 100µg/ml NPs and P-value < 0.05 with 500µg/ml NPs) (Figure 40, 41).

The reduction in metabolic activity of U2OS cells compared to untreated U2OS cells was significantly higher after five days of LbL-NP PC4 and PC5 treatment at all concentrations (P-value < 0.001) (Figure 40, 41). U2OS cells treated with LbL-NPs P4 did not exhibit a significantly different metabolic activity compared to untreated U2OS cells (P-value > 0.05) (Figure 40, 41). However, U2OS cells treated with LbL-NPs P5 had significantly lower metabolic activity compared to untreated U2OS cells (P-value < 0.05 with 100µg/ml NPs and P-value < 0.001 with 500 and 1000µg/ml NPs) (Figure 40, 41).

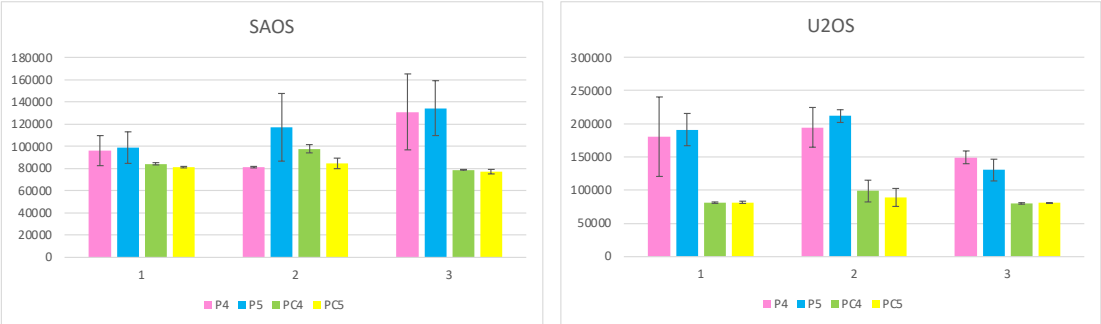

Figure 43: Presto blue results after 24 hours

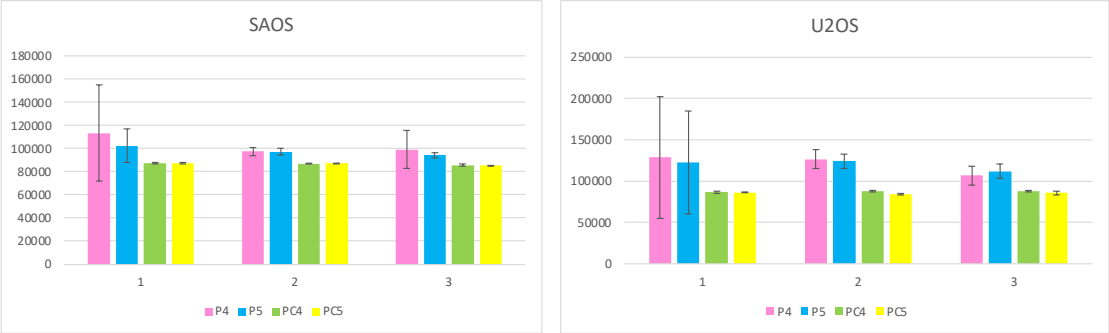

Figure 44: Presto blue results after 5 days

6. DISCUSSION

6.1. CHARACTERIZATION OF MANUFACTURED NPS

DLS, XPS, QCM-D and FTIR-ATR analyses were conducted to characterize the physical and chemical properties of the LbL-NPs, which were fabricated using either pectin or pectin/curcumin.

The zeta potentials of the multi-layered coatings, specifically the P4/P5 and PC4/PC5 samples, showed no significant differences in positive and negative electrolytes. This implies that they exhibit similar electrostatic interaction strengths, resulting in equally effective multi-layered coatings of PLGA-CS polyplexes through LbL assembly.

The LbL-NPs with four layers had an outer CS layer, rendering them positively charged. It's widely recognized that positively charged NPs tend to be more internalized by cells due to favorable electrostatic interactions with the negatively charged cell membrane. Consequently, P4 and PC4 samples are expected to exhibit greater cell internalization compared to P5 and PC5 samples, which have an overall negative charge from the outer HA layer. However, it's noteworthy that a 24-hour treatment of LbL-NP P4 showed the least cytotoxic effects on U2OS cells and did not significantly reduce metabolic activity compared to untreated cells. This contradicts the literature, as increased cell internalization is typically associated with greater cytotoxic effects[82,83].

The QCM-D confirms the results obtained with DLS: it is evident, using this analysis, that there is a significant interaction between the chosen polyelectrolytes, and also it is evident that the adding of curcumin doesn’t change this propriety. The only difference is observed in the 5 layers formulations in which hyaluronic acid provide a negative charge to all the formulation (increasing of the final gap).

FTIR-ATR analysis allowed for a comparison of the chemical characteristics of the four different types of LbL-NPs. Similar absorption peaks were observed in PLGA-CS polyplexes, P4, and P5 samples, such as those around 2250, 2700, and 2800 cm-1, corresponding to C-O, O-H, and C-H stretching of the CH2 groups produced by CS. In P4 and P5, these peaks could also correspond to O-H and C-H bond stretching from pectin (63, 64). Additionally, C-H and O-H stretching peaks were present in PC4 and PC5 samples

around 2300-2800 and 3400-3500 cm-1. These peaks could be attributed to pectin and curcumin.

XPS analysis further characterized the chemical composition of the LbL-NPs and PLGA-CS polyplexes. The O1s analysis of PLGA-CS polyplexes revealed the presence of PLGA, DOX, and CS due to the high At% of 67.69, corresponding to the C=O bonds at 532.37 eV. P4 and P5 samples exhibited similar high At% values, around 75, for C-O bonds, which may correspond to pectin and CS. Furthermore, nitrogen was detected in both XPS surveys of P4 and P5, indicating the presence of CS and DOX due to N-H and C-N bonds. However, P5 had approximately double the At% of nitrogen compared to P4, attributed to the NH2 bonds in HA and CS.

PC5 samples' XPS survey confirmed the presence of nitrogen due to the HA outer layer. This presence was also evident in the O1s analysis of PC5, with a high At% corresponding to the C-O bond at 532.85 eV (66). This bond was also present in pectin and curcumin, highlighting their concentration. In contrast, the XPS survey of PC4 revealed the presence of pectin and curcumin, with the highest At% for C-C bonds at 63.68. Curcumin presence was confirmed in the C1s XPS analysis, as indicated by the C=C bond.

Notably, silicon was detected in all manufactured NPs via XPS analysis, suggesting the presence of contaminants in the samples, although silicon At% levels were low (0.89 to 6.89%). These contaminants may originate from the Eppendorf equipment used in the manufacturing process. Additionally, fluorine was present in the XPS survey of P4 samples, possibly binding primarily to cell wall pectin. However, no fluorine was recorded in the XPS survey of P5, possibly due to the higher concentrations of HA and CS and lower concentrations of pectin in the sample on the XPS films[84].

6.2. ENCAPSULATION & PROLONGED DRUG RELEASE OF DOX AND MIRNA NPS

Both the manufactured miR-NPs and miRD-NPs demonstrated equally high efficacy in encapsulating miR-34a, with a mean encapsulation efficiency (EE) of 99.97%. The lack of significant differences in mean EE between the two formulations (P-value >0.05) was evident. Notably, the manufacturing process for PLGA-CS polyplexes resulted in a superior miR-34a encapsulation efficiency compared to existing PLGA-CS NPs. This

highlights the optimization of the polyplex manufacturing protocol, achieved by incorporating 50uL of miR-34a during polyplex preparation (see Section 3.1). Although miRD-NPs exhibited a slightly lower mean EE for DOX (69.74%) than for miR-34a, the PLGA-CS polyplexes still achieved an effective DOX EE of over 60%, thus minimizing drug wastage and manufacturing costs[35].

To assess the drug release profiles, a one-way ANOVA statistical test with Tukey comparisons was performed on the final two time points of drug release. This analysis aimed to determine whether a drug release plateau was reached. If a plateau was observed, the mean endpoints would not exhibit significant differences (P-value >0.05), indicating that the drug had been entirely released in earlier time points. Conversely, if the mean endpoints differed significantly (P-value <0.05), it suggested ongoing drug release, indicating prolonged release.

Upon analyzing the data, it was observed that two out of the eight pairs of points examined exhibited p-values of less than 0.05. Specifically, the manufactured P4 and PC4 LbL-NPs displayed significantly different mean endpoints (P-value 0.002 and P-value 0.011). Consequently, only these two types of LbL-NPs showed prolonged miR-34a release. Conversely, P5 and PC5 samples did not display significantly different mean endpoints (P-value 0.0611 and P-value 0.173), suggesting that miR-34a was released at earlier time points. This implies that the use of four multi-layered coatings in the LbL assembly on PLGA-CS polyplexes was more effective in achieving prolonged miR-34a release. However, all manufactured LbL-NPs did not exhibit significantly different mean endpoints for DOX release, indicating that none of the LbL-NPs enabled prolonged DOX release. This suggests that DOX is more challenging to encapsulate, as it was released at earlier time points.

6.3. EVALUATION OF CYTOTOXICITY IN THE TWO CELLS LINE

In order to assess the impact of the manufactured LbL-NPs on osteosarcoma cells, a series of cellular assays were conducted, which included the Live/Dead assay and the PrestoBlue assay. These assays were employed to evaluate both the cell viability and metabolic activity of the cells in response to the LbL-NPs.

6.3.1. SAOS-2: NPS HAD NO CYTOTOXIC EFFECTS

The results from the PrestoBlue assay showed that the metabolic activity of SaoS-2 cells treated with all concentrations of the manufactured LbL-NPs for both 24 hours and five days was not significantly different from that of the untreated SaoS-2 cells (P-value >0.05). These findings suggest that the manufactured LbL-NPs did not induce significant cytotoxic effects on the SaoS-2 cells. However, it's important to note that the Live/Dead assay could not be conducted on the SaoS-2 cells due to limited supplies, which highlights a limitation in the study as only the PrestoBlue assay was performed.

6.3.2. U2OS: NPS HAD CYTOTOXIC EFFECTS

In contrast to the SaoS-2 cells, the U2OS cells exhibited reduced metabolic activity and showed signs of apoptotic activity when exposed to the manufactured LbL-NPs, indicating cytotoxic effects. Specifically, when treated with concentrations of 500µg/ml and 1mg/ml, the LbL-NPs significantly reduced the metabolic activity of U2OS cells after five days of treatment (P-value <0.001). Additionally, apoptotic activity and cell death were observed in U2OS cells treated with various concentrations of LbL-NPs at both incubation times.

Notably, among the LbL-NPs, P4 had the least cytotoxic effects on both U2OS and SaoS-2 cells. Live/dead imaging demonstrated that cells treated with LbL-NP P4 experienced the lowest level of cell death during both incubation durations. Furthermore, after 24 hours of treatment with LbL-NP P4, the metabolic activity of both U2OS and SaoS-2 cells was not significantly different from untreated cells (P-values >0.05). These results suggest that the LbL-NPs with four multi-layered nanocoatings of pectin and curcumin are less effective at delivering miR-34a and DOX, and therefore, they have a reduced ability to reach the drug target and induce cytotoxic effects.

6.4. USE OF CURCUMIN IN CANCER TREATMENT

The manufactured LbL-NP PC4 and PC5 led to a decrease in the metabolic activity of U2OS cells when compared to P4 and P5 at all concentrations of NPs. This suggests that

curcumin may play a role in reducing the metabolic activity of osteosarcoma cells[87].It's worth noting that curcumin is believed to exert its anticancer effects by targeting various aspects of mitochondrial function, including glucose metabolism and the production of reactive oxygen species, which are crucial for cancer cell survival and proliferation.

However, it's important to mention that the results of the live/dead assay did not show an increase in cell death in U2OS cells treated with PC4 and PC5 LbL-NPs. This suggests that while curcumin may affect the metabolic activity of osteosarcoma cells, it does not necessarily impact cell viability to the extent of inducing significant cell death. Other factors may also be contributing to the observed reduction in metabolic activity without a corresponding increase in cell death.

These findings indicate the complex and multifaceted nature of curcumin's effects on cancer cells and highlight the need for further research to fully understand its mechanisms of action and its potential as a therapeutic agent in cancer treatment.

6.5. HA: LAST LAYER TO INCREASE CELL VIABILITY

The U2OS cells treated with P5 and PC5 LbL-NPs exhibited a higher level of apoptotic activity and cell death compared to those treated with P4 and PC4 LbL-NPs, both after 24 hours and five days of treatment. These findings support previous research suggesting that hyaluronic acid effectively targets osteosarcoma cells by binding to the CD44 receptor and facilitating receptor-mediated endocytosis. This process allows more LbL-NPs to enter osteosarcoma cells, enabling a greater delivery of miR-34a and DOX to their intended drug targets and subsequently resulting in increased cytotoxicity [91,92].

However, it remains unclear whether the enhanced cytotoxic effect is primarily attributed to the active targeting of hyaluronic acid or to the increased number of multi-layered nanocoatings. The increased number of nanocoatings may enable more efficient transportation of miR-34a and DOX, which, in turn, could lead to a higher concentration of these agents reaching their intended drug targets, thereby exerting synergistic antitumor effects[85,86].

It's worth noting that PC4 and P4 were the only LbL-NPs that demonstrated prolonged release of miR-34a and DOX. Consequently, PC5 and PC5 released most of the drugs at earlier time points, which may have contributed to the heightened cytotoxic effects

observed at the time points used for cell tests. These findings underscore the importance of drug release kinetics in determining the efficacy of these LbL-NPs in cancer therapy.

7. FUTURE DEVELOPMENTS

The cytotoxicity assessment relied on live/dead assay results. However, this method detects non-viable cells through fluorescent reagents exclusive to those with compromised membrane permeability. Consequently, exogenous labeling necessitates incubation for optimal staining, making rapid evaluation challenging. Additionally, staining-induced toxicity can induce cell death, impeding long-term investigations into LbL-NP effects. Furthermore, LbL-NP size determination via transmission electron microscopy was hindered by subpar sample quality. Consequently, assessing LbL-NPs' cell penetration and evasion of the reticuloendothelial system is infeasible.

We demonstrated that manufactured LbL-NPs had no significant cytotoxic impact on SaoS-2 cells compared to untreated ones, implying limited efficacy against osteosarcoma cells. However, live/dead assays weren't conducted on 2D or 3D SaoS-2 cell models due to recurrent culture contamination, resulting in the loss of all cells. Consequently, LbL-NPs may induce cell death but not significantly reduce SaoS-2 cell metabolic activity. Validation may entail live/dead assays on 2D and 3D SaoS-2 cell models.

The cytotoxicity assessment of manufactured LbL-NPs indicates that PC5 and PC5 LbL-NPs exhibit superior cytotoxicity against U2OS cells compared to P4 and PC4. Enhanced cytotoxicity might stem from two factors: effective targeting of osteosarcoma cells by hyaluronic acid or enhanced multi-layered nanocoating through LbL assembly, facilitating miR-34a and DOX transport to drug targets. Therefore, conducting PrestoBlue and live/dead assays on osteosarcoma cells treated with P5 LbL-NPs and four-layered LbL-NPs containing pectin, chitosan, pectin, and hyaluronic acid could provide valuable insights. Additionally, exploring NP internalization via flow cytometry and evaluating cell gene expression pre- and post-LbL-NP treatment, using qRT-PCR to assess gene effects driven by miR-34a, is worth investigating.

8. CONCLUSIONS

This thesis discusses the effective application of nanocarrier systems to deliver tumour suppressive miRNA-34a, Doxorubicin and curcumin simultaneously into in vitro manufactured Osteosarcoma spheroids and two-dimensional cell models. Chitosan and PLGA emerged as ideal materials for nanocarriers in combating Osteosarcoma due to their excellent mechanical properties, biodegradability, biocompatibility, and FDA and EMA approvals. The initial nanoparticles (miR-NPs), comprising Chitosan-PLGA-miR34a NPs, exhibited suitable size, favourable charge for Osteosarcoma application, and efficient miRNA encapsulation while preserving their spherical shape.

The subsequent nanoparticles, miRDx, incorporated Doxorubicin, showing slightly larger sizes. Transmission electron microscopy (TEM) revealed distinct morphological changes, possibly due to the internal presence of drugs. These nanoparticles maintained appropriate size, charge, and efficient encapsulation of miRNA and Doxorubicin.

Finally, Layer-by-Layer nanoparticles (LbL-NPs) were created by nanocoating miRDx-NPs with a pectin layer, in two formulation: with and without pectin, a chitosan layer and a hyaluronic acid layer. LbL-NPs had a larger size but remained suitable in size and charge for Osteosarcoma. TEM images confirmed differences in core morphology compared to miR-NPs, likely due to drug presence. Zeta potential results demonstrated alternating positive and negative charges during layer preparation.

All types of nanoparticles exhibited sustained miRNA and drug release, with gradual release over approximately three days. The nanoparticles were tested on two-dimensional cell models at various cell densities and monoculture Osteosarcoma spheroids. Spheroid size analysis revealed an initial decrease followed by growth, suggesting cell proliferation. Doxorubicin and miRNA-loaded nanoparticles demonstrated enhanced cytotoxicity in two-dimensional cell models due to synergistic antitumor effects.

While spheroid-level differences weren't apparent, the presence of a necrotic core increased with incubation time, indicating more dead cells. Metabolic activity assessment revealed that LbL-NPs were more cytotoxic and interfered with metabolic activity in both cell types and models. They carried miR-34a, Doxorubicin, and Curcumin

effectively to the core without excessive dispersion, potentially due to their natural nanocoating via layer-by-layer assembly.

9. LIST OF FIGURES

10. LIST OF TABLES

11. LIST OF ABBREVIATION

Doxorubicin	DOX
Nanoparticle	NP
Nanoparticle-mediated targeted drug delivery systems	NTDDS
Layer-by-Layer	LbL
MicroRNA	miRNA
MicroRNA-34a	miR-34a
Chitosan	CS
Hyaluronic acid	HA
Poly (lactic-co-glycolic acid)	PLGA
Epithelial-to-mesenchymal transition	EMT
Nuclear factor kappa light chain enhancer of activated B cells	NF-$_k$B
Signal transducer and activator of transcription 3	STAT-3
Encapsulation efficiency	EE
Phosphate buffered saline	PBS
Dulbecco's modified eagle's medium	DMEM
Ultraviolet-Visible	UV-Vis
Human bone osteosarcoma epithelial cells	U2OS
Human primary osteogenic sarcoma	SaoS-2
Fourier-transform infrared Spectroscopy-Attenuated total reflectance	FTIR-ATR
X-ray photoelectron spectroscopy	XPS
Transmission electron microscope	TEM
Two-dimensional	2D
Three-dimensional	3D
Distilled water	dH_2O
Poly (lactic-co-glycolic acid) – Chitosan polyplexes encapsulated with miR-34a	miR-NPs

Poly (lactic-co-glycolic acid) – Chitosan polyplexes encapsulated with miR-34a and doxorubicin	miRD-NPs
Atomic percentage	At%
Binding energy	BE
4’,6-diamidino-2-phenylindole	DAPI
Red fluorescent protein	RFP
Transmission	TRANS

12. REFERENCES

1. Alkekhia, D., Hammond, P. T., & Shukla, A. (2020). Layer-by-Layer Biomaterials for Drug Delivery. https://doi.org/10.1146/annurev-bioeng-060418

2. Ambrosio, L., Raucci, M. G., Vadalà, G., Ambrosio, L., Papalia, R., & Denaro, V. (2021). Innovative biomaterials for the treatment of bone cancer. In International Journal of Molecular Sciences (Vol. 22, Issue 15). MDPI. https://doi.org/10.3390/ijms22158214

3. Bassi, G., Panseri, S., Dozio, S. M., Sandri, M., Campodoni, E., Dapporto, M., Sprio, S., Tampieri, A., & Montesi, M. (2020). Scaffold-based 3D cellular models mimicking the heterogeneity of osteosarcoma stem cell niche. Scientific Reports, 10(1). https://doi.org/10.1038/s41598-020-79448-y

4. Bottai, G., Pasculli, B., Calin, G. A., & Santarpia, L. (2014). Targeting the microRNA-regulating DNA damage/repair pathways in cancer. In Expert Opinion on Biological Therapy (Vol. 14, Issue 11, pp. 1667–1683). Informa Healthcare. https://doi.org/10.1517/14712598.2014.950650

5. Buondonno, I., Gazzano, E., Tavanti, E., Chegaev, K., Kopecka, J., Fanelli, M., Rolando, B., Fruttero, R., Gasco, A., Hattinger, C., Serra, M., & Riganti, C. (2019). Endoplasmic reticulum-targeting doxorubicin: a new tool effective against doxorubicin-resistant osteosarcoma. Cellular and Molecular Life Sciences, 76(3), 609–625. https://doi.org/10.1007/s00018-018-2967-9

6. Cersosimo, F., Lonardi, S., Bernardini, G., Telfer, B., Mandelli, G. E., Santucci, A., Vermi, W., & Giurisato, E. (2020). Tumor-associated macrophages in osteosarcoma: From mechanisms to therapy. In International Journal of Molecular Sciences (Vol. 21, Issue 15, pp. 1–20). MDPI AG. https://doi.org/10.3390/ijms21155207

7. Chaharband, F., Daftarian, N., Kanavi, M. R., Varshochian, R., Hajiramezanali, M., Norouzi, P., Arefian, E., Atyabi, F., & Dinarvand, R. (2020). Trimethyl chitosan-hyaluronic acid nano-polyplexes for intravitreal VEGFR-2 siRNA delivery: Formulation and in vivo efficacy evaluation. Nanomedicine: Nanotechnology, Biology, and Medicine, 26. https://doi.org/10.1016/j.nano.2020.102181

8. Chang, L., Shrestha, S., LaChaud, G., Scott, M. A., & James, A. W. (2015). Review of microRNA in osteosarcoma and chondrosarcoma. In Medical Oncology (Vol. 32, Issue 6). Humana Press Inc. https://doi.org/10.1007/s12032-015-0613-z

9. Corre, I., Verrecchia, F., Crenn, V., Redini, F., & Trichet, V. (2020). The osteosarcoma microenvironment: A complex but targetable ecosystem. In Cells (Vol. 9, Issue 4). MDPI. https://doi.org/10.3390/cells9040976

10. Cosco, D., Cilurzo, F., Maiuolo, J., Federico, C., Di Martino, M. T., Cristiano, M. C., Tassone, P., Fresta, M., & Paolino, D. (2015). Delivery of miR-34a by chitosan/PLGA nanoplexes for the anticancer treatment of multiple myeloma. Scientific Reports, 5. https://doi.org/10.1038/srep17579

11. Cosco, D., Federico, C., Maiuolo, J., Bulotta, S., Molinaro, R., Paolino, D., Tassone, P., & Fresta, M. (2014). Physicochemical features and transfection properties of chitosan/poloxamer 188/poly(D,L-lactide-co-glycolide) nanoplexes. International Journal of Nanomedicine, 9(1), 2359–2372. https://doi.org/10.2147/IJN.S58362

12. Dawidczyk, C. M., Russell, L. M., & Searson, P. C. (2014). Nanomedicines for cancer therapy: State-of-the-art and limitations to pre-clinical studies that hinder future developments. In Frontiers in Chemistry (Vol. 2, Issue AUG). Frontiers Media S. A. https://doi.org/10.3389/fchem.2014.00069

13. Deiss-Yehiely, E., Brucks, S. D., Boehnke, N., Pickering, A. J., Kiessling, L. L., & Hammond, P. T. (2022). Surface Presentation of Hyaluronic Acid Modulates Nanoparticle-Cell Association. Bioconjugate Chemistry, 33(11), 2065–2075. https://doi.org/10.1021/acs.bioconjchem.2c00412

14. Djafari, J., Fernández-Lodeiro, J., Santos, H. M., Lorenzo, J., Rodriguez-Calado, S., Bértolo, E., Capelo-Martínez, J. L., & Lodeiro, C. (2020). Study and preparation of multifunctional poly(L-lysine)@hyaluronic acid nanopolyplexes for the effective delivery of tumor suppressive mir-34a into triple-negative breast cancer cells. Materials, 13(23), 1–9. https://doi.org/10.3390/ma13235309

15. Dorfman, H. D., & Czerniak, B. (1995). Bone cancers. Cancer, 75(1 S), 203–210. https://doi.org/10.1002/1097-0142(19950101)75:1+<203::AID-CNCR2820751308>3.0.CO;2-V

16. Ducy, P., Schinke, T., & Karsenty, G. (2000). The Osteoblast: A Sophisticated Fibroblast under Central Surveillance. In Source: Science, New Series (Vol. 289, Issue 5484).

17. Eaton, B. R., Schwarz, R., Vatner, R., Yeh, B., Claude, L., Indelicato, D. J., & Laack, N. (2021). Osteosarcoma. Pediatric Blood and Cancer, 68(S2). https://doi.org/10.1002/pbc.28352

18. Fernandez-Piñeiro, I., Badiola, I., & Sanchez, A. (2017). Nanocarriers for microRNA delivery in cancer medicine. In Biotechnology Advances (Vol. 35, Issue 3, pp. 350–360). Elsevier Inc. https://doi.org/10.1016/j.biotechadv.2017.03.002

19. Findenig, G., Kargl, R., Stana-Kleinschek, K., & Ribitsch, V. (2013). Interaction and structure in polyelectrolyte/clay multilayers: A QCM-D study. Langmuir, 29(27), 8544–8553. https://doi.org/10.1021/la400880a

20. Genedy, H. H., Delair, T., & Montembault, A. (2022). Chitosan Based MicroRNA Nanocarriers. In Pharmaceuticals (Vol. 15, Issue 9). MDPI. https://doi.org/10.3390/ph15091036

21. Giordano, A., & Tommonaro, G. (2019). Curcumin and cancer. In Nutrients (Vol. 11, Issue 10). MDPI AG. https://doi.org/10.3390/nu11102376

22. Goyal, R., Kapadia, C. H., Melamed, J. R., Riley, R. S., & Day, E. S. (2018). Layer-by-Layer Assembled Gold Nanoshells for the Intracellular Delivery of miR-34a. Cellular and Molecular Bioengineering, 11(5), 383–396. https://doi.org/10.1007/s12195-018-0535-x

23. Hameed, M., Horvai, A. E., & Jordan, R. C. K. (2020). Soft Tissue Special Issue: Gnathic Fibro-Osseous Lesions and Osteosarcoma. Head and Neck Pathology, 14(1), 70–82. https://doi.org/10.1007/s12105-019-01094-2

24. Hastuti, B., & Kurniawati, M. (2020). Synthesis and Characterization of Pectin Membrane as a Matrix for Curcumin Sustained-Release. IOP Conference Series: Materials Science and Engineering, 833(1). https://doi.org/10.1088/1757-899X/833/1/012069

25. He, C., Xiong, J., Xu, X., Lu, W., Liu, L., Xiao, D., & Wang, D. (2009). Functional elucidation of MiR-34 in osteosarcoma cells and primary tumor samples. Biochemical and Biophysical Research Communications, 388(1), 35–40. https://doi.org/10.1016/j.bbrc.2009.07.101

26. Hu, Z., Wen, S., Huo, Z., Wang, Q., Zhao, J., Wang, Z., Chen, Y., Zhang, L., Zhou, F., Guo, Z., Liu, H., & Zhou, S. (2022). Current Status and Prospects of Targeted Therapy for Osteosarcoma. In Cells (Vol. 11, Issue 21). MDPI. https://doi.org/10.3390/cells11213507

27. Jin, S., Xu, H. guang, Shen, J. nan, Chen, X. wu, Wang, H., & Zhou, J. guo. (2009). Apoptotic effects of curcumin on human osteosarcoma U2OS cells. Orthopaedic Surgery, 1(2), 144–152. https://doi.org/10.1111/j.1757-7861.2009.00019.x

28. Kapadia, C. H., Ioele, S. A., & Day, E. S. (2020). Layer-by-layer assembled PLGA nanoparticles carrying miR-34a cargo inhibit the proliferation and cell cycle progression of triple-negative breast cancer cells. Journal of Biomedical Materials Research - Part A, 108(3), 601–613. https://doi.org/10.1002/jbm.a.36840

29. Kean, T., & Thanou, M. (2010). Biodegradation, biodistribution and toxicity of chitosan. In Advanced Drug Delivery Reviews (Vol. 62, Issue 1, pp. 3–11). https://doi.org/10.1016/j.addr.2009.09.004

30. Kim, J. H., Moon, M. J., Kim, D. Y., Heo, S. H., & Jeong, Y. Y. (2018). Hyaluronic acid-based nanomaterials for cancer therapy. In Polymers (Vol. 10, Issue 10). MDPI AG. https://doi.org/10.3390/polym10101133

31. Lahr, C. A., Landgraf, M., Wagner, F., Cipitria, A., Moreno-Jiménez, I., Bas, O., Schmutz, B., Meinert, C., Cavalcanti, A. D. S., Mashimo, T., Miyasaka, Y., Holzapfel, B. M., Shafiee, A., McGovern, J. A., & Hutmacher, D. W. (2022). A humanised rat model of osteosarcoma reveals ultrastructural differences between bone and mineralised tumour tissue. Bone, 158. https://doi.org/10.1016/j.bone.2021.116018

32. Li, S., Xiong, Y., & Zhang, X. (2017). Poloxamer surface modified trimethyl chitosan nanoparticles for the effective delivery of methotrexate in osteosarcoma. Biomedicine and Pharmacotherapy, 90, 872–879. https://doi.org/10.1016/j.biopha.2017.04.004

33. Lima, F. T., Seba, V., Silva, G., Torrezan, G. S., Polaquini, C. R., Pinhanelli, V. C., Baek, S. J., Fachin, A. L., Regasini, L. O., & Marins, M. (2018). The curcumin analog CH-5 exerts anticancer effects in human osteosarcoma cells via modulation of transcription factors p53/Sp1. International Journal of Molecular Sciences, 19(7). https://doi.org/10.3390/ijms19071909

34. Lorenzo, J., Horowitz, M., & Choi, Y. (2008). Osteoimmunology: Interactions of the bone and immune system. In Endocrine Reviews (Vol. 29, Issue 4, pp. 403–440). https://doi.org/10.1210/er.2007-0038

35. Lu, B., Lv, X., & Le, Y. (2019). Chitosan-modified PLGA nanoparticles for control-released drug delivery. Polymers, 11(2). https://doi.org/10.3390/polym11020304

36. Mackie, E. J. (2003). Osteoblasts: Novel roles in orchestration of skeletal architecture. In International Journal of Biochemistry and Cell Biology (Vol. 35, Issue 9, pp. 1301–1305). Elsevier Ltd. https://doi.org/10.1016/S1357-2725(03)00107-9

37. Maroof, H., Salajegheh, A., Smith, R. A., & Lam, A. K. Y. (2014). Role of microRNA-34 family in cancer with particular reference to cancer angiogenesis. In Experimental and Molecular Pathology (Vol. 97, Issue 2, pp. 298–304). Academic Press Inc. https://doi.org/10.1016/j.yexmp.2014.08.002

38. Mialou, V., Philip, T., Kalifa, C., Perol, D., Gentet, J. C., Marec-Berard, P., Pacquement, H., Chastagner, P., Defaschelles, A. S., & Hartmann, O. (2005). Metastatic osteosarcoma at diagnosis: Prognostic factors and long-term outcome - The French pediatric experience. In Cancer (Vol. 104, Issue 5, pp. 1100–1109). https://doi.org/10.1002/cncr.21263

39. Miao, J., Wu, S., Peng, Z., Tania, M., & Zhang, C. (2013). MicroRNAs in osteosarcoma: Diagnostic and therapeutic aspects. In Tumor Biology (Vol. 34, Issue 4, pp. 2093–2098). IOS Press BV. https://doi.org/10.1007/s13277-013-0940-7

40. Miele, D., Xia, X., Catenacci, L., Sorrenti, M., Rossi, S., Sandri, G., Ferrari, F., Rossi, J. J., & Bonferoni, M. C. (2021). pharmaceutics Chitosan Oleate Coated PLGA Nanoparticles as siRNA Drug Delivery System. https://doi.org/10.3390/pharmaceutics

41. Misaghi, A., Goldin, A., Awad, M., & Kulidjian, A. A. (2018). Osteosarcoma: A comprehensive review. In SICOT-J (Vol. 4). EDP Sciences. https://doi.org/10.1051/sicotj/2017028

42. Misra, R., Acharya, S., & Sahoo, S. K. (2010). Cancer nanotechnology: Application of nanotechnology in cancer therapy. In Drug Discovery Today (Vol. 15, Issues 19–20, pp. 842–850). https://doi.org/10.1016/j.drudis.2010.08.006

43. Moore, D. D., & Luu, H. H. (2014). Osteosarcoma. Cancer Treatment and Research, 162, 65–92. https://doi.org/10.1007/978-3-319-07323-1_4

44. Morton, S. W., Shah, N. J., Quadir, M. A., Deng, Z. J., Poon, Z., & Hammond, P. T. (n.d.). Osteotropic therapy via targeted Layer-by-Layer nanoparticles NIH Public Access.

45. Munoz-Garcia, J., Jubelin, C., Loussouarn, A., Goumard, M., Griscom, L., Renodon-Cornière, A., Heymann, M. F., & Heymann, D. (2021). In vitro three-dimensional cell cultures for bone sarcomas. In Journal of Bone Oncology (Vol. 30). Elsevier GmbH. https://doi.org/10.1016/j.jbo.2021.100379

46. Novello, C., Pazzaglia, L., Conti, A., Quattrini, I., Pollino, S., Perego, P., Picci, P., & Benassi, M. S. (2014). P53-dependent activation of microRNA-34a in response to etoposide-induced DNA damage in osteosarcoma cell lines not impaired by dominant negative p53 expression. PLoS ONE, 9(12). https://doi.org/10.1371/journal.pone.0114757

47. Nugent, M. (2014). MicroRNA function and dysregulation in bone tumors: The evidence to date. Cancer Management and Research, 6(1), 15–25. https://doi.org/10.2147/CMAR.S53928

48. Ognjanovic, S., Olivier, M., Bergemann, T. L., & Hainaut, P. (2012). Sarcomas in TP53 germline mutation carriers: A review of the IARC TP53 database. Cancer, 118(5), 1387–1396. https://doi.org/10.1002/cncr.26390

49. O'Neal, J. T., Dai, E. Y., Zhang, Y., Clark, K. B., Wilcox, K. G., George, I. M., Ramasamy, N. E., Enriquez, D., Batys, P., Sammalkorpi, M., & Lutkenhaus, J. L. (2018). QCM-D Investigation of Swelling Behavior of Layer-by-Layer Thin Films upon Exposure to Monovalent Ions. Langmuir, 34(3), 999–1009. https://doi.org/10.1021/acs.langmuir.7b02836

50. Palmini, G., Marini, F., & Brandi, M. L. (2017). What is new in the miRNA world regarding osteosarcoma and chondrosarcoma? In Molecules (Vol. 22, Issue 3). MDPI AG. https://doi.org/10.3390/molecules22030417

51. Parhi, P., Mohanty, C., & Sahoo, S. K. (2012). Nanotechnology-based combinational drug delivery: An emerging approach for cancer therapy. In Drug Discovery Today (Vol. 17, Issues 17–18, pp. 1044–1052). https://doi.org/10.1016/j.drudis.2012.05.010

52. Peng, S. F., Lee, C. Y., Hour, M. J., Tsai, S. C., Kuo, D. H., Chen, F. A., Shieh, P. C., & Yang, J. S. (2014). Curcumin-loaded nanoparticles enhance apoptotic cell death of U2OS human osteosarcoma cells through the Akt-Bad signaling pathway. International Journal of Oncology, 44(1), 238–246. https://doi.org/10.3892/ijo.2013.2175

53. Petit, D., Lavrijsen, R., Lee, J., Mansell, R., Fernández-Pacheco, A., & Cowburn, R. P. (2016). Systematic layer-by-layer characterization of multilayers for three-dimensional data storage and logic. Nanotechnology, 27(15). https://doi.org/10.1088/0957-4484/27/15/155203

54. Puluhulawa, L. E., Joni, I. M., Elamin, K. M., Mohammed, A. F. A., Muchtaridi, M., & Wathoni, N. (2022). Chitosan–Hyaluronic Acid Nanoparticles for Active Targeting in Cancer Therapy. In Polymers (Vol. 14, Issue 16). MDPI. https://doi.org/10.3390/polym14163410

55. Sakurai, N., Iwamoto, S., Miura, Y., Nakamura, T., Matsumine, A., Nishioka, J., Nakatani, K., & Komada, Y. (2013). Novel p53 splicing site mutation in Li-Fraumeni-like syndrome with osteosarcoma. Pediatrics International, 55(1), 107–111. https://doi.org/10.1111/j.1442-200X.2012.03641.x

56. Salamanna, F., Contartese, D., Maglio, M., & Fini, M. (2016). A systematic review on in vitro 3D bone metastases models: A new horizon to recapitulate the native clinical scenario? In Oncotarget (Vol. 7, Issue 28). www.impactjournals.com/oncotarget/

57. Salerno, M., Cenni, E., Fotia, C., Avnet, S., Granchi, D., Castelli, F., Micieli, D., Pignatello, R., Capulli, M., Rucci, N., Angelucci, A., Fattore, A. Del, Teti, A., Zini, N., Giunti, A., & Baldini, N. (2010). Bone-Targeted Doxorubicin-Loaded Nanoparticles as a Tool for the Treatment of Skeletal Metastases. In Current Cancer Drug Targets (Vol. 10).

58. Salgado, A. J., Coutinho, O. P., & Reis, R. L. (2004). Bone tissue engineering: State of the art and future trends. In Macromolecular Bioscience (Vol. 4, Issue 8, pp. 743–765). https://doi.org/10.1002/mabi.200400026

59. Sampson, V. B., Yoo, S., Kumar, A., Vetter, N. S., & Kolb, E. A. (2015). MicroRNAs and Potential Targets in Osteosarcoma: Review. In Frontiers in Pediatrics (Vol. 3). Frontiers Media S.A. https://doi.org/10.3389/fped.2015.00069

60. Sato, T., Mello, D., Vasconcelos, L., Valente, A., & Borges, A. (2020). Chitosan-based coacervate polymers for propolis encapsulation: Release and cytotoxicity studies. International Journal of Molecular Sciences, 21(12), 1–15. https://doi.org/10.3390/ijms21124561

61. Shafei, A., El-Bakly, W., Sobhy, A., Wagdy, O., Reda, A., Aboelenin, O., Marzouk, A., El Habak, K., Mostafa, R., Ali, M. A., & Ellithy, M. (2017). A review on the efficacy and toxicity of different doxorubicin nanoparticles for targeted therapy in metastatic breast cancer. In Biomedicine and Pharmacotherapy (Vol. 95, pp. 1209–1218). Elsevier Masson SAS. https://doi.org/10.1016/j.biopha.2017.09.059

62. Sikavitsas, V. I., Temeno, J. S., & Mikos, A. G. (2001). Biomaterials and bone mechanotransduction. In Biomaterials (Vol. 22).

63. Tian, Y., Zhang, Y. Z., & Chen, W. (2014). MicroRNA-199a-3p and microRNA-34a regulate apoptosis in human osteosarcoma cells. Bioscience Reports, 34(4), 479–485. https://doi.org/10.1042/BSR20140084

64. Wang, J., Liu, S., Shi, J., Li, J., Wang, S., Liu, H., Zhao, S., Duan, K., Pan, X., & Yi, Z. (2019). The Role of miRNA in the Diagnosis, Prognosis, and Treatment of Osteosarcoma. In Cancer Biotherapy and Radiopharmaceuticals (Vol. 34, Issue 10, pp. 605–613). Mary Ann Liebert Inc. https://doi.org/10.1089/cbr.2019.2939

65. Wang, S. Y., Hu, H. Z., Qing, X. C., Zhang, Z. C., & Shao, Z. W. (2020). Recent advances of drug delivery nanocarriers in osteosarcoma treatment. In Journal of Cancer (Vol. 11, Issue 1, pp. 69–82). Ivyspring International Publisher. https://doi.org/10.7150/jca.36588

66. Wu, K., Yu, B., Li, D., Tian, Y., Liu, Y., & Jiang, J. (2022). Recent Advances in Nanoplatforms for the Treatment of Osteosarcoma. In Frontiers in Oncology (Vol. 12). Frontiers Media S.A. https://doi.org/10.3389/fonc.2022.805978

67. Wu, X., Zhong, D., Gao, Q., Zhai, W., Ding, Z., & Wu, J. (2013). MicroRNA-34a inhibits human osteosarcoma proliferation by downregulating ether à go-go 1 expression. International Journal of Medical Sciences, 10(6), 676–682. https://doi.org/10.7150/ijms.5528

68. Wu, Y., Rashidpour, A., Almajano, M. P., & Metón, I. (2020). Chitosan-Based drug delivery system: Applications in fish biotechnology. In Polymers (Vol. 12, Issue 5). MDPI AG. https://doi.org/10.3390/POLYM12051177

69. Xi, Y., Jiang, T., Yu, Y., Yu, J., Xue, M., Xu, N., Wen, J., Wang, W., He, H., Shen, Y., Chen, D., Ye, X., & Webster, T. J. (2019). Dual targeting curcumin loaded alendronatehyaluronan- octadecanoic acid

micelles for improving osteosarcoma therapy. International Journal of Nanomedicine, 14, 6425–6437. https://doi.org/10.2147/IJN.S211981

70. Yang, X., Zhang, Y., Malichewe, C., Shi, Z., Wang, L., Lu, Z., & Guo, X. (2019). Chitosan nanoparticle mediated upregulation of microRNA34a expression to suppress the proliferation, migration, invasion of MDA-MB-231 cells. Journal of Drug Delivery Science and Technology, 52, 1061–1069. https://doi.org/10.1016/j.jddst.2019.06.020

71. Yu, D., Zhang, S., Feng, A., Xu, D., Zhu, Q., Mao, Y., Zhao, Y., Lv, Y., Han, C., Liu, R., & Tian, Y. (2019). Methotrexate, doxorubicin, and cisplatinum regimen is still the preferred option for osteosarcoma chemotherapy: A meta-analysis and clinical observation. In Medicine (United States) (Vol. 98, Issue 19). Lippincott Williams and Wilkins. https://doi.org/10.1097/MD.0000000000015582

72. Zhang, G., Li, Y., Xu, J., & Xiong, Z. (2020). Advances in the role of miRNAs in the occurrence and development of osteosarcoma. Open Medicine (Poland), 15(1), 1003–1011. https://doi.org/10.1515/med-2020-0205

73. Zhang, J., Yan, Y. G., Wang, C., Zhang, S. J., Yu, X. H., & Wang, W. J. (2015). MicroRNAs in osteosarcoma. In Clinica Chimica Acta (Vol. 444, pp. 9–17). Elsevier B.V. https://doi.org/10.1016/j.cca.2015.01.025

74. Zou, Y., Huang, Y., Yang, J., Wu, J., & Luo, C. (2017). MIR-34a is downregulated in human osteosarcoma stem-like cells and promotes invasion, tumorigenic ability and self-renewal capacity. Molecular Medicine Reports, 15(4), 1631–1637. https://doi.org/10.3892/mmr.2017.6187

75. Xiongwei Deng et al., Hyaluronic acid-chitosan nanoparticles for co-delivery of MiR-34a and doxorubicin in therapy against triple negative breast cancer. Biomaterials 35 (2014) 4333-4344, doi: doi: 10.1016/j.biomaterials.2014.02.006

76. Lingegowda EC, Kumar JK, Prasad AGD, Zarei M, Gopal S. FTIR Spectroscopic studies on cleome gynandra - comparativr analysis of functional group before and after extraction. ROMANIAN J BIOPHYS. 2012;22:137–43

77. Promega. QuantiFluor® RNA System Quick Protocol FB199 2023 [Available from: https://www.promega.co.uk/products/rna-analysis/dna-and-rna-quantitation/quantifluor-rna-system/?catNum=E3310. [

78. Merck. IR Spectrum Table and chart 2023 [Available from: https://www.sigmaaldrich.com/GB/en/technical-documents/technical-article/analytical-chemistry/photometry-and-reflectometry/ir-spectrum-table.

79. Drabczyk A, Kudłacik-Kramarczyk S, Głąb M, Kędzierska M, Jaromin A, Mierzwiński D, Tyliszczak B. Physicochemical Investigations of Chitosan-Based Hydrogels Containing Aloe Vera Designed for Biomedical Use. Materials (Basel). 2020;13(14):3073. Available from DOI: 10.3390/ma13143073.

80. Thermo Fisher Scientific. Oxygen X-ray photoelectron spectra, oxygen electron configuration, and other elemental information. 2023 [Available from: https://www.thermofisher.com/uk/en/home/materials-science/learning

81. Thermo Fisher Scientific. Carbon X-ray photoelectron spectra, carbon electron configuration, and other elemental information 2023 [Available from: https://www.thermofisher.com/uk/en/home/materials-science/learning-center/periodic-table/non-metal/carbon.html.

82. Yue Z, Lv P, Wang L, Su Z, Ma G, et al. Surface Charge Affects Cellular Uptake and Intracellular Trafficking of Chitosan-Based Nanoparticles. Biomacromolecules. 2011;12(7):2440-6. Available from DOI: 10.1021/bm101482r.

83. Verma A, Stellacci F. Effect of surface properties on nanoparticle-cell interactions. Small. 2010;6(1):12-21. Available from DOI: 10.1002/smll.200901158. [30/06/2023]
84. Luo J, Ni D, Li C, Du Y, Chen Y. The relationship between fluoride accumulation in tea plant and changes in leaf cell wall structure and composition under different fluoride conditions. Environmental Pollution. 2021;270(1):116283. Available from DOI: 10.1016/j.envpol.2020.116283.

85. Najjary S, Mohammadzadeh R, Mansoori B, et al. Combination therapy with miR-34a and doxorubicin synergistically induced apoptosis in T-cell acute lymphoblastic leukemia cell line. Med Oncol. 2021;38:142. Available from DOI: 10.1007/s12032-021-01578-8.

86. Zhao Y, Tu M, Yu Y, Wang W, Chen Q, Qiu J, et al. Combination therapy with bioengineered miR-34a prodrug and doxorubicin synergistically suppresses osteosarcoma growth. Biochemical Pharmacology. 2015;98(4): 602-13. Available from DOI: 10.1016/j.bcp.2015.10.015.

87. Jung KH, Lee JH, Park JW, Moon SH, Cho YS, Choe YS, Lee KH. Effects of curcumin on cancer cell mitochondrial function and potential monitoring with ^{18}F-FDG uptake. Oncol Rep. 2016;35(2):861-8. Available from DOI: 10.3892/or.2015.4460.

88. Aggarwal S, Ichikawa H, Takada Y, Sandur SK, Shishodia S, Aggarwal BB. Curcumin (diferuloylmethane) down-regulates expression of cell proliferation and antiapoptotic and metastatic gene products through suppression of IκBα kinase and Akt activation. Molecular Pharmacology. 2006;69(1): 195–206. Available from DOI: 10.1124/mol.105.017400.

89. Zhang Y, Ding C, Wang J, et al. Prognostic significance of CD44V6 expression in osteosarcoma: a meta-analysis. Journal of Orthopaedic Surgery and Research. 2015;10:187. Available from DOI: 10.1186/s13018-015-0328-z.

90. Rao NV, Yoon HY, Han HS, Ko H, Son S, Lee M, et al. Recent developments in hyaluronic acid-based nanomedicine for targeted cancer treatment. Expert Opinion on Drug Delivery. 2016;13(2):239-52. Available from DOI: 10.1517/17425247.2016.1112374.

91. Muntimadugu E, Kumar R, Saladi S, Rafeeqi TA, Khan W. CD44 targeted chemotherapy for co-eradication of breast cancer stem cells and cancer cells using polymeric nanoparticles of salinomycin and paclitaxel. Colloids and Surfaces B: Biointerfaces. 2016;143:532-46. Available from DOI: 10.1016/j.colsurfb.2016.03.075.

92. Salahpour Anarjan F. Active targeting drug delivery nanocarriers: Ligands. Nano-Structures & Nano-Objects. 2019;19:100370. Available from DOI: 10.1016/j.nanoso.2019.100370.

93. https://www.pharmacy180.com/article/microscopic-anatomy-%28bone-cells%29-3487/

94. Jason L. Ferguson, DO, MBA Bone cancer: diagnosis and treatment principles 2018

95. Hu, Z.; Wen, S.; Huo, Z.; Wang, Q.; Zhao, J.; Wang, Z.; Chen, Y.; Zhang, L.; Zhou, F.; Guo, Z.; et al. Current Status and Prospects of Targeted Therapy for Osteosarcoma. *Cells* **2022**, *11*, 3507. https://doi.org/ 10.3390/cells11213507

96. Sindhu Doppalapudi, Anjali Jain, Abraham J. Domb & Wahid Khan (2016): Biodegradable polymers for targeted delivery of anti-cancer drugs, Expert Opinion on Drug Delivery, DOI: 10.1517/17425247.2016.1156671